Accessory phase perspectives for ore-forming processes and magmatic sulphide exploration in the Labrador Trough, northern Québec, Canada

*W.D. Smith[1,2], W.D. Maier[1], J.C.Ø. Andersen[3], D.D. Muir[1], E.T. Mansur[4,5], & I. Bliss[6]

[1]School of Earth and Environmental Sciences, Cardiff University, CF10 3AT, United Kingdom

[2]Department of Earth Sciences, Herzberg Laboratories, Carleton University, Ottawa, Ontario, K1S 5B6, Canada

[3]Camborne School of Mines, University of Exeter, Penryn Campus, Penryn TR10 9FE, United Kingdom

[4]Sciences de la Terre, Université du Québec à Chicoutimi, Québec, G7H 2B1, Canada

[5]Geological Survey of Norway, PO Box 6315 Torgarden, Trondheim, 7491, Norway

[6]Northern Shield Resources, 500-55 Metcalfe Street, Ottawa, Ontario K1P 6L5, Canada

*Corresponding author: williamsmith3@cunet.carleton.ca

Abstract

The compositions of resistant indicator minerals are diagnostic of their original host environment. They may be used to fingerprint different types of mineral deposit as well as vector towards them. We have characterised the composition of apatite and Fe-Ti oxides in variably-mineralised mafic-ultramafic rock units of the Montagnais Sill Complex in the Labrador Trough to assess their suitability for vectoring magmatic sulphide occurrences. Two broad types of apatite were identified: (i) fluoro- to hydroxy-apatite ($Cl/[Cl+F] < 0.2$); and (ii) chloro- to hydroxy apatite ($Cl/[Cl+F] > 0.5$). The former reflects variable degrees of degassing and Cl-loss during Rayleigh fractionation and is not indicative of Ni-Cu-mineralisation or host rock. The latter exists only in sulphidic olivine cumulate units and thus, may be used to vector similar rock types in the Labrador Trough. Ilmenite is the dominant oxide, except for the upper parts of differentiated gabbroic sills in which titanomagnetite is dominant. Magnetite occurs only as a secondary phase in serpentinised olivine cumulates and is not discriminative for magmatic sulphides. Ilmenite and titanomagnetite in the sulphidic olivine-bearing units have characteristically high Mg (~ 1,000-10,000 ppm), Cr (~ 100-1,000 ppm), Ni (~ 10-1,000 ppm), and Cu (~ 1-10,000 ppm) concentrations relative to those from other rock units. Their composition is consistent with Fe-Ti oxides derived from evolved sulphide melts in ultramafic-hosted Ni-Cu-(PGE) sulphide deposits and thus may be used to vector towards similar magmatic sulphide occurrences in the Labrador Trough.

Keywords: apatite, Fe-Ti oxides, Labrador Trough, Canada, magmatic sulphide, PGE

1. Introduction

Resistant indicator minerals (RIMs) are widely used in the early stages of exploration for a range of commodities to delineate areas of heightened prospectivity (Averill, 2001; McClenaghan, 2011; Gent *et al.* 2011). The application of geochemical discrimination diagrams for RIMs to an exploration programme is based on our empirical understanding of the relationship between the RIM and the sought-after commodity. Optimal RIMs are those that are: (i) common minerals in the relevant rock types; (ii) robust and invulnerable to hydrothermal alteration; (iii) sensitive to the environment from which they crystallised; (iv) accessible, either from the relevant rock types or associated detrital repositories; and (v) easy to identify, separate, and analyse (Gent *et al.* 2011; Layton-Matthews *et al.* 2014).

Apatite and Fe-Ti oxides are ideal candidates for RIMs since they are both robust and ubiquitous accessory phases in a range of magmatic (magmatic sulphide [Boudreau & McCallum 1989; 1992; Dupuis & Beaudoin 2011; Dare *et al.* 2012; 2014; Raič *et al.* 2019], kimberlite [Wyatt *et al.* 2004; McClenaghan *et al.* 2007; Kaminsky & Belousova, 2009]; Kiruna-type [Chai *et al.* 2014; Broughm *et al.* 2017; La Cruz, 2019]; carbonatite rare earth element (REE) deposits [Simandl *et al.* 2017]), (magmatic)-hydrothermal (Cu-porphyry [Bouzari *et al.* 2016; Pisiak *et al.* 2017; Chapman *et al.* 2018]; volcanogenic massive sulphide deposits [Makvandi *et al.* 2015; 2016]; skarn deposits [McQueen *et al.* 1998; Nadoll *et al.* 2015]; iron-oxide-copper-gold deposits [Corriveau *et al.* 2007; Lypaczewski *et al.* 2013]), and sedimentary (exhalative [Bryson, 2017]; uranium deposits [Makvandi *et al.* 2017]) ore deposits. The composition of these phases reflects the conditions from which they crystallised, meaning they may be used to fingerprint different types of mineral deposit and their associated ore-forming processes (Belousova *et al.* 2002; Dupuis & Beaudoin 2011; Nadoll *et al.* 2014; Mao *et al.* 2016) as well as vector towards undiscovered ore deposits (Ames *et al.* 2007; Pisiak *et al.* 2014; O'Sullivan *et al.* 2020).

The Labrador Trough in northern Québec is an ideal location for the deployment of RIMs in exploration programmes because: (i) it represents a vast, glaciated terrane with abundant lakes and streams as well as limited rock exposure; and (ii) it has a diverse array of mineral occurrences from which accessory phases will possess distinct chemical characteristics (Clark & Wares 2005). The Palaeoproterozoic Montagnais Sill Complex (MSC) is a mafic-ultramafic sill complex that hosts several styles of magmatic sulphide mineralisation in the Labrador Trough (see Clark & Wares 2005; Smith *et al.* 2020a; 2020b). In the present study, we have characterised the compositions of accessory apatite and Fe-Ti oxides in variably-mineralised mafic-ultramafic rock units from the Idefix PGE-Cu (Smith *et al.* 2020a) and Huckleberry Cu-Ni-(PGE) (Smith *et al.* 2020b) prospects. We show that those associated with magmatic sulphides in gabbro-peridotite sills are compositionally distinct and may be used to delineate Ni-Cu-mineralised rock units in the Labrador Trough.

2. Accessory phases as indicator minerals in magmatic sulphide mineral systems

2.1. Apatite

Apatite [$Ca_5(PO_4)_3(F, Cl, OH)$] has a chemical formula of $^{IX}M1_2{}^{VII}M2_3(^{IV}TO_4)_3X$, whereby Ca^{2+} cations occupy the *M1* (~ 40% and 1.06 Å) and *M2* (~ 60% at 1.18 Å) sites and monovalent anions (F^-, Cl^-, and OH^-) occupy the *X-site* (Pasero *et al.,* 2010; Mao *et al.* 2016). The crystal structure of apatite allows for a range of substitution reactions, including: (1) the replacement of Ca^{2+} in the *M1* and *M2* sites by divalent, and trivalent cations, including Sr, Mn, Y, REEs, Na, Mg, and Ba; (2) the replacement of PO_4^{3-} in the *TO* site by anionic complexes (including VO_4^{3-}, SiO_4^{4-}, SO_4^{2-}); and (3) the modification of the monovalent anions in the *X*-site (Pasero *et al.* 2010 and references therein).

Several authors have used apatite as a petrogenetic tracer in igneous systems (see Bruand *et al.* 2017 and references therein) and more recently, to trace ore-forming processes (*e.g.,* Belousova *et al.* 2002; Mao *et al.* 2016; Raič *et al.* 2018; Andersson *et al.* 2019). The minor and trace element concentrations of apatite reflect the conditions of crystallisation and are particularly sensitive to the redox and SiO_2 activities of the host magma (Hughes & Rakovan 2015). Studies of magmatic sulphides have used the halogen budget of apatite to determine its origin and hence, the genetic origin of co-existing ore minerals (*e.g.,* Boudreau & McCallum, 1989; Willmore *et al.* 2000; Gál *et al.* 2013; Schisa *et al.* 2015; Raič *et al.* 2018). The relative proportions of anions are monitored by: (1) the melt ± fluid compositions; (2) presence of other F- and Cl-bearing phases; and (3) the intensive parameters of the system (Harlov 2015). Cumulus apatite nucleating according to Rayleigh fractionation is typically fluorapatite, since during degassing, a silicate magma becomes preferentially enriched in F relative to Cl according to their melt/vapour partition coefficients (*e.g.,* Boudreau & McCallum, 1989; Mathez & Webster, 2005). The presence of chlorapatite is ascribed to Cl-addition by Cl-rich magmatic-hydrothermal fluids, which are potentially capable of transporting metal cations, such as the PGEs (see Boudreau, 2019 and references therein).

2.2. Iron-titanium oxides

Magnetite (Fe_3O_4), titanomagnetite ($Fe_{3-x}Ti_xO_4$; the Ti-rich endmember is known as ulvöspinel), and ilmenite ($FeTiO_3$) are common constituents in mafic-ultramafic rocks as well as magmatic sulphide ores. In the magnetite-ulvöspinel series, the crystal structure ranges from ideal magnetite [$^{T}(Fe^{3+})^{M}(Fe^{2+}Fe^{3+})O_4$] to ideal ulvöspinel [$^{T}(Fe^{2+})^{M}(Fe^{2+}Ti^{4+})O_4$], and titanomagnetite represents phases occurring within this series (Bosi *et al.* 2009). Ferrous and ferric iron cations in magnetite and titanomagnetite can be isomorphically replaced by divalent (*e.g.,* Ni, Co, Cu, Zn), trivalent (*e.g.,* Cr, REEs, V), and tetravalent (*e.g.,* Ti, high-field strength elements; HFSEs; Liang *et al.* 2013; Sievwright, 2017) cations. Ilmenite has a crystal structure of $^{T}(Fe^{2+})^{M}(Ti^{4+})O_3$, where divalent cations (*e.g.,* Mg^{2+}, Ca^{2+}, Na^{2+}) preferentially replace Fe^{2+} at the *T*-site, and trivalent (*e.g.,* Cr, Mn, REEs) and tetravalent (*e.g.,* HFSEs) cations preferentially replace Ti^{4+} at the *M*-site (*e.g.,* Wilson *et al.* 2005; Van Kan Parker *et al.* 2011).

Several studies detail the application of Fe-Ti oxides as petrogenetic traces in magmatic sulphide mineral systems (*e.g.,* Dupuis & Beaudoin, 2011; Dare *et al.* 2012; 2014; Nardoll *et al.* 2014; Boutroy *et al.* 2014). The Fe-Ti oxides, and in particular magnetite, can form under a wide variety of conditions where the degree of concentration of a foreign cation reflects: (i) the concentration of the element in the parent melt or fluid; (ii) the supersaturated crystal assemblage; (iii) the partition coefficient of the element into the magnetite lattice; and (iv) the intensive parameters (*e.g.,* temperature, pressure, fugacity) of the host system (Dupuis & Beaudoin 2011; Dare *et al.* 2012). The capability of Fe-Ti oxides to precipitate from silicate melt, Fe-rich and Cu-rich sulphide melt, and hydrothermal fluid, means its composition is particularly diagnostic of its crystallising environment (Dare *et al.* 2012; 2014).

3. Geological background

3.1. Regional setting

The Labrador Trough (or New Québec Orogen) is a northwest-oriented orogenic belt, extending > 850 km from the south of Ungava Bay to the Grenville Front (Fig. 1A; Hoffman 1990; Henrique-Pinto *et al.* 2019). The belt represents the suture between the Archaean Superior craton and the so-called Core Zone during the closure of the Manikewan Ocean at ~ 1.8 Ga (Hoffman 1990; Wardle & Van Kranendonk 1996; Corrigan *et al.* 2009). The supracrustal rocks of the Labrador Trough comprise a thick sequence of Palaeoproterozoic (~ 2.17-1.87 Ga) metavolcanic and metasedimentary units (Clark & Wares, 2005 and references therein) that constitute the foreland of the New Québec Orogeny. Previous workers have sub-divided the supracrustal sequence into three cycles, each bound by an erosional unconformity (*e.g.,* Hoffman 1990; Clark & Wares, 2005). Cycle 1 comprises parautochthonous epi-continental to platform sediments mostly deposited before 2142 ± 4 Ma (Clark 1984). Cycle 2 consists of greenschist-facies, allochthonous volcano-sedimentary sequences intruded and extruded by tholeiitic magmas of the MSC at ~ 1884 ± 1.6 Ma (Findlay *et al.* 1995; Machado *et al.* 1997). Cycle 3 represents allochthonous syn-orogenic molasse-style deposits that crop-out in the east.

3.2. Nature and mineralisation of the Montagnais Sill Complex

The MSC represents the easternmost segment of the Circum-Superior large igneous province (Barager & Scoates 1981). The parent magmas intruded and extruded Cycle 2 sedimentary rock units between 1.88-1.87 Ga (Findlay *et al.* 1995). The Hellancourt and Willbob basalt formations, occurring in the northern and southern Labrador Trough, respectively, represent the extrusive component of the MSC. These formations are thought to be regional equivalents and direct feeder dykes between intrusive and extrusive rocks have been observed (Wares & Goutier 1990). The intrusive rocks of the MSC have been divided into four main sill types, which is reflected in the four main types of magmatic sulphide mineralisation documented by Clark & Wares (2005) in the MSC. The sill types and their respective mineralisation is described below.

Type A. Sub-volcanic ferropicritic sills and flows occur in the northern Qarqasiaq Igneous Complex in the northern Labrador Trough (Mungall 1998). These units comprise serpentinised peridotitic cumulates overlain by variably-grained gabbroic unis. These sills can host massive to disseminated sulphides at their base, with grades of 0.4-4.1% Ni, 0.15-0.73% Cu, 0.15-2.3 g/t Pd, and 0.67-1.0 g/t Pt (Mungall 1998; Clark & Wares 2005). However, Kastek *et al.* (2020) have shown that the Qarqasiaq Igneous Complex may form part of the southern extremity of the Cape Smith Belt and not the Labrador Trough. The implication being that these sulphide occurrences may not be representative of the MSC and as such, have not been included in this study.

Type B. Differentiated aphyric gabbro sills, often with peridotitic cumulate units, are most common in the Hurst and Howse lithotectonic zones in the southern Labrador Trough. From the base to the top, these sills include: (i) partially serpentinised olivine cumulates; (ii) olivine gabbro; (iii) aphyric gabbro; (iv) oxide-rich gabbro; and (v) granophyric gabbro. Massive to disseminated sulphides can sometimes occur in the basal olivine cumulate units and can possess grades of 0.2-1% Cu, 0.2-1.2% Ni, and 0.4-1.1 g/t Pt+Pd over several metres. Mineralised rocks are characterised by low Cu/Ni (~ 0.5-3), moderate Cu/Pd (~ 8,000-15,000), and variable Pd/Ir (~ 50-1,000) values, relative to other types. Examples of this type of occurrence include Lac Retty (394 tons at 0.99% Cu, 0.66% Ni, 1.13 g/t Pt+Pd; Clark 1989; 1991; Clark & Wares 2005), Hope's Advance (Wares & Mungall 1997), and Huckleberry (Smith *et al.* 2020b). At Hope's Advance and Huckleberry, sulphide melt has percolated downward from the gabbro-peridotite sill into the glomeroporphyritic gabbro footwall (Wares & Mungall 1997; Smith *et al.* 2020b; 2021b).

Type C. Glomeroporphyritic gabbro sills are considered to be the oldest sill type in the Labrador Trough, and they generally occur in the Baby, Howse, and Hurst lithotectonic zones (Findlay *et al.* 1995; Clark & Wares 2005). This sill type is characterised by a fine- to medium-grained gabbroic groundmass that hosts extremely variable abundances of variably-sized plagioclase glomerocrysts, that may locally create an anorthosite. The base of this sill type, hereafter referred to as the pyroxenitic glomeroporphyritic unit (PGU), contains little-to-no plagioclase glomerocrysts (< 10 vol.% glomerocrysts). The glomeroporphyritic gabbros can host massive to disseminated sulphides with peak grades of ~ 3% Cu, 0.8% Ni, and 1 g/t Pt+Pd over ~ 10 m. Globular sulphides sometimes occur in the PGU. Mineralised rocks are characterised by variable Cu/Ni (~ 0.5-20), high Cu/Pd (> 10,000), and moderate Pd/Ir (~ 50-200) values, relative to other types. Examples of this type of occurrence include Lepage (1.09 Mt at 2.02% Cu and 0.45% Ni; Lacroix & Darling 1991; Clark & Wares 2005), Lac Redcliff (0.97 Mt at 2.09% Cu and 0.51% Ni; Lacroix & Darling 1991; Clark & Wares 2005), and Huckleberry (Smith *et al.* 2020b).

Type D. Aphyric (or equigranular) gabbro sills typically occur in the Gerido lithotectonic zone in the northern Labrador Trough. The gabbros are texturally and mineralogically comparable to *Type B* aphyric gabbros, yet they differ in that they do not possess basal cumulate units. Instead, they possess stratiform gabbroic pegmatite units that are intermittently traceable across the host sill. Spatially associated with these pegmatitic units are disseminated or globular sulphides, with grades of 0.2-1 g/t Pt+Pd and ~ 0.5% Cu over 10-20 m. Mineralised rocks are characterised by moderate Cu/Ni (~ 0.5-5), low Cu/Pd (< 10,000), and variable Pd/Ir (~ 50-500) values, relative to other types. Examples of this type of occurrence include Lac Lafortune (2.54 g/t Pt, 1.65 g/t Pd, and 1.45% Cu from grab samples; Clark & Wares 2005), Paladin (4.6 g/t Pd and 0.76 g/t Pt over 2 m; Girard & Gagnon 2005; Clark & Wares 2005), and Idefix (Smith *et al.* 2020a).

In addition, several low-grade post-magmatic hydrothermal Cu±(PGE-Ni-Au-Ag) sulphide occurrences have been identified in ultramafic, volcanic, and metasedimentary rocks that are spatially associated with orthomagmatic occurrences (see Clark & Wares 2005).

3.3. Summary of the Idefix PGE-Cu prospect

The Idefix PGE-Cu prospect (*Type D*) is located ~ 75 km west of the town of Kuujjuaq and is situated in the Gerido lithotectonic zone (Fig. 1B) (Clark & Wares, 2005; Smith *et al.,* 2020a). It represents a > 400-m-thick stack of fine- to medium-grained aphyric gabbro sills that intrude meta-arenitic and metapelitic rocks of the Upper Baby Formation (Vaillancourt *et al.* 2012; Smith *et al.* 2020a). A horizon of disseminated sulphides (~ 0.2-1 g/t Pt+Pd+Au and ~ 0.1-0.5% Cu over ~ 10-20 m) occurs in the centre of the sill complex and globular sulphides occur at the base, both of which are spatially associated with stratiform gabbroic pegmatite units (Smith *et al.* 2021b). Mineralised rocks are characterised by Cu/Pd < 5,000, Pd/Ir ~ 100-500, and crustal-like δ^{34}S values (-0.3-3.8‰; Smith *et al.* 2020a; 2021a). Clark & Wares (2005) proposed that disseminated sulphides in *Type D* occurrences precipitated from magmatic-hydrothermal fluids based on their spatial relationship with gabbroic pegmatites and the general absence of basal sulphide accumulations. However, Smith *et al.* (2020a) proposed that sulphide melt was transported from its site of origin, where it segregated in response to crustal contamination and attained *R* factors exceeding 10,000.

3.4. Summary of the Huckleberry Cu-Ni-(PGE) prospect

The Huckleberry Cu-Ni-(PGE) prospect (*Types B* and *C*) is located ~ 100 km north of the town of Schefferville and is situated in the Hurst lithotectonic zone (Fig. 1C) (Clark & Wares 2005; Smith *et al.* 2020b). It represents two ~ 100-m-thick sequences of glomeroporphyritic gabbros divided by a ~ 200-m-thick gabbroic sill that from the base upwards comprises: (i) basal olivine cumulates: (ii) olivine gabbro; (iii) aphyric gabbro; (iv) titanomagnetite gabbro; and (v) granophyric gabbro (Vaillancourt *et al.* 2016; Smith *et al.* 2020b). In addition, protrusions of olivine cumulate extend from the gabbro-peridotite sill into the underlying glomeroporphyritic gabbros, hereafter referred to as the footwall olivine cumulates (Fig. 1C). Disseminated to net-textured sulphides occur in the olivine cumulate units and also in the underlying glomeroporphyritic gabbro units (~ 0.2-1.5% Cu, ~ 0.2-1.2% Ni, and 0.4-1.1 g/t Pt+Pd+Au over several metres). Moreover, globular sulphides occur at the base of the sill stack in the PGU. Mineralised olivine cumulates and glomeroporphyritic gabbros are characterised by Cu/Pd > 5,000, Pd/Ir < 300, and variable δ^{34}S values (-4.5-3.2‰; Smith *et al.* 2020b; 2021a). It is hypothesised that sulphide melt segregated in response to crustal contamination (*R* factor = 1,000-5,000) at depth (*i.e.,* a staging chamber or feeder conduit) and was transported to its current position (Clark & Wares 2005; Smith *et al.* 2020b; 2021a). Alternatively, Laurent (1995) proposed that these sulphides are volcanic in origin, having been derived from circulating hydrothermal fluids.

4. Samples and methods

Apatite and Fe-Ti oxides in representative polished sections and mounts from Idefix (*n* = 4) and Huckleberry (*n* = 18) were petrographically characterised by optical (Leica MZ12s optical microscope) and electron microscopy (Zeiss Sigma HD Field Emission Gun Analytical Scanning Electron Microscope equipped with two Oxford Instruments 150 mm^2 energy dispersive spectrometers) at the School of Earth and Environment Sciences at Cardiff University. The sections were prepared from drill cores sampled by the first author in the Autumn of 2019 and detailed in previous works (Smith *et al.* 2020a; 2020b). The reader is referred to the supplementary materials for details regarding the location of samples used in this study. Element maps were produced using an accelerating voltage of 20 kV, a 120 µm final aperture in high current mode, with a nominal beam current of 8.5 nA and a dwell time of 5,000-20,000 µm, at a working distance of 8.9 mm.

Compositional analyses of these phases were performed over four analytical sessions using a JEOL JXA-8200 electron probe microanalyzer at the Camborne School of Mines, University of Exeter.

Analyses were made using wavelength dispersive spectrometers only and were calibrated to natural mineral standards supplied by P&H Developments and Astimex Scientific and quantified using the CITZAF ϕρZ method of Armstrong (1995) implemented for JEOL by Paul Carpenter. Apatite was analysed at 15 kV, 30 nA and with a beam diameter of 10 µm. Fluorine and chlorine were systematically analysed first with 40 s count times to minimise variations due to beam damage. It is well documented that F*Kα* and Cl*Kα* X-ray counts may vary with grain composition and orientation as well as EPMA operating conditions and electron-beam exposure times (Stormer *et al.* 1993; Goldoff *et al.* 2012; Stock *et al.* 2015). Fluorine standards are problematic, as fluorite (Das *et al.* 2017) as well as fluorapatite (Stormer *et al.* 1993) display systematic variance under electron beam exposure. We chose the Durango fluorapatite in order to best match the expected variations of the apatite. We consider the variance arising from halogen migration to be within the total analytical uncertainty that also includes variability in the standard measurements and data reduction procedures ($2\sigma = 0.2$-0.5 wt.% F). Standards analyses and results are provided in the supplementary materials. Apatite data ($n = 48$ from Idefix; $n = 139$ from Huckleberry) were recalculated using the method of Deer *et al.* (1992) and Fe-Ti oxide data were recalculated using a charge balance allocation of Fe to match the stoichiometry of the minerals. In addition, the interference of Ti-Kβ on V-Kα was measured at 0.34 wt.% V_2O_3 in 100 wt.% TiO_2 and subtracted manually from each mineral analysed.

Analyses of Fe-Ti oxides at Huckleberry (88 ilmenite, 16 titanomagnetite, and 3 magnetite from 15 samples) were performed at LabMaTer, Université du Québec à Chicoutimi (UQAC; Canada) using an Excimer 193-nm RESOlution M-50 laser ablation system (Australian Scientific Instrument) equipped with a double volume cell S-155 (Laurin Technic) and coupled with an Agilent 7900 mass spectrometer. Alteration and grain size prevented analysis of Fe-Ti oxides in Idefix aphyric gabbros. The analytical procedure followed that detailed in Duran *et al.* (2020). A stage movement speed of 10 µm/s, a dwell time of 7.5 ms, a laser frequency of 15 Hz, and a fluence of 5 J/cm^2 were used to analyse the Fe-Ti oxide grains. Line scans across the surface of Fe-Ti oxides grains were made with beam sizes of 55 or 44 µm, depending on grain size. The gas blank was measured for 30 s before switching on the laser for at least 60 s. The ablated material was carried into the ICP-MS by an argon-helium gas mix at a rate of 0.8 to 1 L/min for Ar and 350 mL/min for He, and 2 mL/min of nitrogen was also added to the mixture. Data reduction was carried out using the Iolite package for Igor Pro software (Paton *et al.* 2011).

The following isotopes were quantified: ^{24}Mg, ^{27}Al, ^{44}Ca, ^{45}Sc, ^{49}Ti, ^{51}V, ^{53}Cr, ^{55}Mn, ^{57}Fe, ^{59}Co, ^{60}Ni, ^{65}Cu, ^{66}Zn, ^{71}Ga, ^{74}Ge, ^{89}Y, ^{90}Zr, ^{93}Nb, ^{95}Mo, ^{118}Sn, ^{139}La, ^{172}Yb, ^{178}Hf, ^{181}Ta, ^{182}W, and ^{208}Pb. In addition, ^{29}Si, ^{31}P, and ^{34}S were monitored to ensure that the measured signal represented pure oxide. Silicate and sulphide inclusions encountered during laser ablation were excluded from the signal during data reduction. According to Dare *et al.* (2012), polyatomic interferences of ^{90}Zr from ^{50}Ti^{40}Ar, ^{50}V^{40}Ar, and ^{50}Cr^{40}Ar; ^{92}Zr from ^{52}Cr^{40}Ar; and ^{93}Nb from ^{53}Cr^{40}Ar are negligible in magnetite, and corrections are not required.

Internal standardisation was based on ^{57}Fe using Fe concentrations determined for the corresponding grain during EPMA compositional analysis. Calibration followed that described in Dare *et al.* (2014) and Duran *et al.* (2016). GSE-1g, a natural basalt glass fused and doped with most elements at 300-500 ppm, supplied by the U.S. Geological Survey (USGS), was used to calibrate for all elements using preferred values from the GeoReM database (Jochum *et al.* 2005). In addition, GSD-1g and G-probe 6, which are respectively a synthetic glass and a natural basalt glass (both supplied by the USGS), and BC28, which is a natural magnetite from the Main magnetite layer of the Bushveld Complex (supplied by LabMaTer), were used as quality control reference materials to monitor the calibration of GSE-1g. All unknown and standard measurements are reported in the supplementary materials together with time-signal diagrams showing compositional homogeneity of analysed oxides.

5. Results

5.1. Apatite petrography and compositions

Apatite is present in low modal abundances (< 1 vol.%) in each of the analysed rock types and shows no systematic variation with the sulphide content of the host rock. Subhedral apatite is a common accessory phase in units comprising globular sulphides (~ 0.2-0.3 vol.%; Fig. 2A-B), occurring: (i) interstitially to plagioclase and pyroxene; (ii) within the amphibolitised margins of sulphides; and (iii) as inclusions within sulphide phases. The grains (~ 270-11,200 μm^2) often occur as clusters of several grains. Anhedral apatite is less prevalent (< 0.1 vol.%) in the Idefix aphyric gabbro units (~ 450-33,000 μm^2; Fig. 2C).

In the Huckleberry gabbro-peridotite sill, the modal abundance of apatite in the olivine cumulate units at the base is < 0.1 vol.%, whereas the modal abundance of apatite in the granophyric gabbro at the top is ~ 0.5 vol.%. In olivine cumulate units, anhedral apatite has distinct Cl-rich (generally the cores) and Cl-poor zones (*i.e.,* OH-rich; generally the rims; see supplementary materials), ranging in size from ~180-8,200 μm^2 (Fig. 2D-E). Apatite grains are rare in glomeroporphyritic gabbros (< 0.1 vol.%; ~ 180-2,600 μm^2). Apatite grains in the titanomagnetite and granophyric gabbro units cluster in proximity to Fe-Ti oxides and have the largest average grain sizes (~ 1,200-22,100 μm^2; Fig. 2F-G).

Apatite compositions are summarised in Table 1 and fully reported in the supplementary materials. Most analysed grains have low (< 1 wt.%) Na_2O, MgO, Al_2O_3, SiO_2, MnO, FeO, SrO, and TiO_2 concentrations. Apatite from Idefix aphyric gabbros generally show good compositional overlap, whereby those spatially associated with globular sulphides range from fluorapatite (~ 1.2-3.0 wt.% F) to F-OH apatite (~ 0.4-1.2 wt.% OH), and those associated with disseminated sulphides are generally F-OH apatite (~ 1.0-1.2 wt.% OH and 1.2-1.5 wt.% F; Fig. 3). Apatite grains from Idefix are Cl-poor (< 0.3 wt.%) and show no discernible compositional zonation.

Three types of apatite were identified within the Huckleberry lithotypes (Fig. 3): (1) subhedral to euhedral fluorapatite (~ 2.2-3.8 wt.% F, < 0.6 wt.% Cl, and < 0.5 wt.% OH) hosted in the upper gabbro-peridotite sill; (2) subhedral fluorapatite to F-Cl-OH apatite (~ 1.6-3.8 wt.% F, ~ 0.1-1.6 wt.% Cl, and < 0.6 wt.% OH) hosted amongst the basal PGU globular sulphides; and (3) intercumulus Cl-OH apatite (< 1 wt.% F, ~ 0.3-4.6 wt.% Cl, and ~ 0.3-1.5 wt.% OH) hosted amongst net-textured sulphides in the olivine cumulate units.

5.2. Iron-titanium oxide petrography and compositions

Iron-titanium oxides occur in all mafic-ultramafic units as accessory phases and as major phases in the titanomagnetite and granophyric gabbro units. Iron-titanium oxide compositions are summarised in Table 2 and fully reported in the supplementary materials. Time-signal diagrams (see supplementary materials) show that the reported elements are present in solid solution, where the large spot size negates the effect of mineral exsolution. The compositions of oxides are illustrated as multi-element diagrams, in which elements are normalised to bulk continental crust (Column 12 of Table 9 in Rudnick and Gao 2003; Dare *et al.* 2012) and ordered from left to right according to increasing compatibility into magnetite (Dare *et al.* 2014). This order is favourable due to the diverse environment from which Fe-Ti oxides may crystallise and bulk continental crust is selected as the normalisation reservoir since Fe-Ti oxides typically crystallise from evolved silicate melts more similar in composition to the bulk continental crust.

In all the Idefix aphyric gabbros, very fine-grained (< 100 µm in diameter), anhedral ilmenite is partially to completely replaced by titanite and rutile (Fig. 4A-B). No magnetite or titanomagnetite was identified in these units.

In the PGU at Huckleberry, anhedral ilmenite (< 500 µm in diameter; ~ 1 vol.%) occurs along sulphide-silicate grain boundaries, where it is partially replaced by titanite (Fig. 4C). Clusters of ilmenite-titanite grains are spatially associated with satellite sulphide disseminations. Iron oxides are relatively rare in the overlying glomeroporphyritic gabbros (< 0.1 vol.%) and generally occur with disseminated sulphides (Fig. 4D). The ilmenite grains are rich in HFSE (120-1,273 ppm Zr, 7-42 ppm Hf, 83-523 ppm Nb, and 4-31 ppm Ta), Sn, Mn, Ti, V, and Cr and poor in Si, Ca, Al, Ga, and Mg (Fig. 5A). Copper concentrations are generally < 5 ppm, Co concentrations span a narrow range of 14-31 ppm and Ni concentrations range from 6-19 ppm. Ilmenite analysed in the mineralised glomeroporphyritic gabbro is comparable in composition to those of the PGU, yet generally comprise lower Si, Ca, and Ni concentrations.

In the olivine cumulate units, anhedral ilmenite (< 3 mm in diameter; ~ 0.5-3 vol.%) and subordinate titanomagnetite (< 5 mm in diameter) with ilmenite exsolution lamellae are spatially associated with net-textured sulphides (Fig. 4E-I). Ilmenite in the olivine-bearing units has similar HFSE, Si, Ca, Al, Sn Mn, Ti, V, and Cr concentrations to those of the PGU (Fig. 5B-D). However, those spatially associated with sulphides have relatively higher Cu and Ni concentrations. Titanomagnetite in the footwall olivine cumulates have lower Si, Ca, and HFSE concentrations and higher Al, Cu, Mg, Ni, and Cr concentrations, relative to titanomagnetite in the upper part of the gabbro-peridotite sill (Fig. 5E).

Iron-titanium oxides are a trace accessory phase in the olivine and aphyric gabbro intervals yet become major constituents of the titanomagnetite and granophyric gabbro units (~ 10-15 vol.%). In the titanomagnetite gabbro, anhedral titanomagnetite (< 2 mm in diameter) with ilmenite exsolution lamellae and finer anhedral ilmenite are spatially associated with very sparsely disseminated sulphides (chalcopyrite > pyrite > pyrrhotite; Fig. 4J-K). In the granophyric gabbro, coarse-grained (< 5 mm in diameter) titanomagnetite and subordinate ilmenite are partially replaced by titanite and spatially associated with fluorapatite. Ilmenite grains are similar in composition to those of the glomeroporphyritic units in that they have low relative Si, Ca, Al, Ga, and Mg concentrations, and high relative Mn, Ti, and V concentrations (Fig. 5F). Ilmenite in the titanomagnetite gabbro has higher Nb and Ta concentrations, and lower Zr and Hf concentrations relative to those of the granophyric gabbro. Nickel and Cr concentrations are close to, or below, the detection limit. Titanomagnetite in the titanomagnetite gabbro has similar Zr, Hf, Al, Ti, Co, and V concentrations, lower Ga, Mn, Zn, and Ni concentrations, and higher Si, Ca, Y, and Ge concentrations compared to those of the overlying granophyric gabbro.

Magnetite predominantly occurs in the sulphide-bearing olivine cumulate units, where it is observed as stringers that cross-cut cumulate silicates or partially replacing Fe-sulphides (< 0.5 vol.%; Fig. 4L). Due to its commonly very small grain size, magnetite was only able to be analysed in the footwall olivine cumulates, where it is characterised by low relative Si, Ca, HFSE, Sc, Sn, Ga, Mn, Ti, V, and Cr concentrations and high relative Ge, Cu, Zn, Co, and Ni concentrations (Fig. 5E).

6. Discussion

6.1. Halogen variations in apatite

Variations in the halogen budget of apatite can be explained by several processes: (i) apatite tend to become progressively F-rich during syn-magmatic degassing since Cl preferentially partitions into a co-existing vapour phase with respect to F; (ii) chlorapatite is thought to derive from syn-magmatic Cl mobilisation, whereby migrating Cl-rich vapours redissolve in vapour-undersaturated melts; and (iii) hydroxyapatite forms as a result of alteration or metamorphic processes in which Cl is lost and OH is gained (Boudreau *et al.* 1986; Boudreau & McCallum 1989; Andersen *et al.* 1998; Boudreau & McCallum 1992; Mathez & Webster 2005; Schisa *et al.* 2015). Alternatively, Liu *et al.* (2021) proposed that Fe-REE-poor chlorapatite amongst sulphide ores at Jinchuan may have crystallised directly from Fe-REE-depleted, Cl-bearing sulphide melts.

It has been proposed that Idefix-type PGE-rich disseminated sulphides derived from magmatic-hydrothermal fluids based on the absence of basal sulphide accumulations and the close spatial relationship between sulphides and stratiform gabbroic pegmatites (Clark & Wares 2005). Smith *et al.* (2020a) argued that these sulphides at Idefix represent entrained and disaggregated sulphide globules that initially segregated in response to crustal contamination. The latter argument is supported by: (i) the presence of globular sulphides at the base of the sill; (ii) the compositional and mineralogical similarities between disseminated and globular sulphides; (iii) relatively unevolved whole-rock Pd/Ir (< 500) and undepleted Cu/Pd (< 5,000) values; and (iv) crustal δ^{34}S (-0.3-3.8‰) values (Smith *et al.* 2020a; 2021a). If these sulphides were instead derived from magmatic-hydrothermal fluids, one may expect spatially-associated apatite to be chlorapatite. However, we show that apatite compositions in aphyric Idefix gabbros overlap along the OH-F sideline regardless of the presence of sulphides (Fig. 3), consistent with variable degrees of degassing.

Sulphides at the base of differentiated gabbro-peridotite sills, that sometimes extend into their footwalls, are thought to have been entrained from their site of segregation, where they formed in response to crustal contamination (Clark & Wares 2005; Smith *et al.* 2020b; 2021a). Alternatively, Laurent (1995) proposed that these sulphides are volcanic in origin and precipitated from circulating hydrothermal fluids. At Huckleberry, apatite in the glomeroporphyritic units and upper parts of the gabbro-peridotite sill are generally F-rich with minor Cl-addition, similar to apatite from Munni Munni (Boudreau & Hoatson 2004) and Skaergaard (McBirney & Sonnenthal 1990). At these locations, a decrease in Cl/F and OH/F values are ascribed to progressive fluid or vapour exsolution during crystallisation prior to apatite saturation. Relatively anomalous Cl-rich apatite in the glomeroporphyritic gabbro footwall is comparable to those analysed in the olivine cumulate units at Huckleberry (Fig. 3). The implication is that these Cl-rich apatite grains may be genetically related to the gabbro-peridotite sill and not the glomeroporphyritic gabbro sill; a similar conclusion was determined for disseminated sulphides in this unit (see Smith *et al.* 2020b). Several anhedral apatite grains in the olivine cumulate units display sector zoning of Cl-rich (generally cores) and OH-rich (generally rims) zones, consistent with the leaching of Cl from intercumulus chlorapatite during post-magmatic interaction with serpentine-related and(or) metamorphic fluids (see Boudreau & McCallum 1992). The original chlorapatite may have precipitated from intercumulus melt that became enriched in Cl during the dissolution of Cl-bearing vapours (Boudreau *et al.* 1986) or precipitated directly from Cl-bearing sulphide melts (Liu *et al.* 2021). We suggest that the apatite crystallised from Cl-bearing intercumulus silicate melt since chlorapatite was not identified amongst any other sulphide assemblage. However, we believe these fluids are not responsible for the introduction or enrichment of PGE in these units, on the basis of magmatic Pd/Ir (< 300) and Pd/Pt (~ 2-3) values, evidence for the downward percolation of sulphide melt, and the lack of correlation between PGE concentrations and Cl content.

6.2. Formation of sulphide-associated Fe-Ti oxides: crystallisation from silicate or sulphide melts?

It was previously thought that Fe-Ti oxides were unlikely to crystallise directly from sulphide melts due to the high silicate/sulphide partition coefficient of lithophile elements, particularly Ti ($D^{sil/sul}$ ~ 0.05; Naldrett 1969; Dare *et al.* 2012). It has been known since 1969 that magnetite may precipitate from sulphide melt at ~ 1,050°C when the cotectic between magnetite and monosulphide solid solution (*mss*) is established (Naldrett 1969). This observation offered an explanation as to why magnetite is often observed associated with sulphide minerals in relatively unaltered mafic-ultramafic rock units. However, the occurrence of more titaniferous phases (ilmenite and titanomagnetite) associated with primary sulphides requires diffusion of Ti from co-existing silicates magma into the sulphide-derived magnetite (Prichard *et al.* 2004; Dare *et al.* 2012). Dare *et al.* (2012) have argued that titanomagnetite may crystallise directly from sulphide melt if the parent magmas are sufficiently rich in Ti, yet it remains unclear whether ilmenite could form in this way (Duran *et al.* 2016).

At Huckleberry, the composition of sulphide-associated ilmenite and titanomagnetite is characteristic of Fe-Ti oxides that have crystallised from evolved *mss* (Fig. 6A-B; Dare *et al.* 2012), consistent with entrainment of fractionated sulphide melt from depth (Smith *et al.* 2020b). These Fe-Ti oxides typically occur at sulphide-silicate grain boundaries and thus, may have formed by the interaction between sulphide-derived magnetite and Ti-bearing silicate melt (*e.g.,* Naldrett 1969; Duran *et al.* 2020). The residual heat from the bracketing glomeroporphyritic gabbros may have slowed the cooling rate of the nested gabbro-peridotite sill and resulted in intercumulus melt convection and Ti-enrichment of sulphide-derived magnetite. It remains unclear whether ilmenite could crystallise directly from sulphide melt.

6.3. Composition of Fe-Ti oxides in the titanomagnetite and granophyric gabbros in the upper gabbro-peridotite sill

Iron-titanium oxides are commonly observed in the upper parts of differentiated intrusions (*e.g.,* Bushveld Complex; Klemm *et al.* 1982; Skaergaard, Wager & Brown 1968; Koillismaa, Karinen *et al.* 2015; Panzhihua, Pang *et al.* 2008; Xinjie, Tan *et al.* 2015; Lac Doré, Mathieu 2019; Sonju Lake, Maes *et al.* 2007) because they typically become saturated late in the crystallisation sequence of typical parent magmas. Thermodynamic modelling of the Hellancourt basalts has shown that Fe-Ti oxides become saturated after ~ 68% fractional crystallisation once the residual magma has attained ~ 2.5-3 wt.% TiO_2 (Ciborowski *et al.* 2017; Smith *et al.* 2020b; 2021a). These results are consistent with the stratigraphic occurrence of Fe-Ti oxides and the borehole geochemical patterns in the gabbro-peridotite sill at Huckleberry (Smith *et al.* 2020b). The titanomagnetite and granophyric gabbro units primarily comprise titanomagnetite with trellis-like ilmenite exsolution lamellae and subordinate ilmenite with minor magnetite exsolution lamellae. This assemblage is characteristic of sub-solidus redistribution of cations according to the temperature-dependent exchange of $Fe^{2+} + Ti^{4+} \rightarrow 2Fe^{3+}$ between titanomagnetite and ilmenite solid solution pairs (Buddington & Lindsley 1964; Sauerzapf *et al.* 2008; Tan *et al.* 2015). At the Sept Iles, Lac Saint Jean, and Lac des Iles intrusions, researchers have shown that ilmenite preferentially incorporates HFSEs, W, and Cu, while co-existing titanomagnetite preferentially incorporates Al, Ge, Ni, and Cr (Méric 2011; Néron 2011; Dare *et al.* 2012; Duran *et al.* 2016). These observations are consistent with the trace element distribution amongst ilmenite-titanomagnetite pairs in the upper gabbro-peridotite sill (Fig. 5).

Several authors have documented the occurrence of (titano)magnetite gabbro overlain by granophyric gabbro via gradational contacts in the upper parts of strongly differentiated sills and layered intrusions. The formation of the oxides could represent: (i) the final product of fractional crystallisation (*e.g.,* Skaergaard, Wager 1960; Mt Kilkenny, Jaques 1975; Kevitsa, Mutanen 1997); (ii) segregation of a late-stage immiscible Si-rich melt from a conjugate Fe-rich melt (*e.g.,* Skaergaard, McBirney & Nakamura 1974; Bushveld, Reynolds 1985; Sept Iles, Namur *et al.* 2012; Raftsund Intrusion, Coint *et al.* 2020); (iii) crystallisation from a differentiated melt that migrated upward from the crystallisation front (*e.g.,* Skaergaard, McBirney 1980); or (iv) a partial melt of the bracketing country rocks (*e.g.,* Basistoppen sill, Naslund 1987). In the upper gabbro-peridotite sill, Fe-Ti oxides in the titanomagnetite gabbro are rich in Ca, Y, Ti, Zr, Hf, Mo, Sn, Cu, and V relative to those from the granophyric gabbro, consistent with the $D^{\text{Fe-Ti-rich liquid/Si-rich liquid}}$ values for these elements (Veksler & Charlier 2015 and references therein). However, several elements (*e.g.,* Al, Nb, Ta, Zn) are not distributed according to their experimentally determined partition coefficients. We propose the granophyric gabbro derived from the siliceous residue of a strongly differentiated tholeiitic magma on the basis of gradual upward increases in grain size as well as upward-increasing SiO_2, Na_2O, K_2O, and incompatible trace element concentrations.

6.4. Occurrence of magnetite

Magnetite is a rare accessory phase in mafic-ultramafic rocks of this study. It primarily occurs as minor veins in serpentinised olivine-bearing units at Huckleberry and was likely derived from the reaction:

$$6Fe_2SiO_4 + 7H_2O = 3Fe_3Si_2O_5(OH)_4 + Fe_3O_4 + H_2$$

olivine + water → serpentine + magnetite

Magnetite is also observed replacing Fe-sulphides in the olivine-bearing units at Huckleberry, which likely reflects the following reactions (Li *et al.* 2004):

$$2.53FeS_{(po)} + 0.47Fe^{2+} + 3H_2O \rightarrow Fe^{2+}Fe^{3+}{}_2O_{4\,(mgn)} + 2.53HS^- + 3.47H^+$$

$$CuFeS_{(ccp)} + 2Fe^{2+} + 4H_2O \rightarrow Fe^{2+}Fe^{3+}{}_2O_{4\,(mgn)} + Cu^{2+} + 2HS^- + 4H^+ + H_2$$

$$Fe_4Ni_5S_{9\,(pn)} + 6.65Fe^{2+} + 14.2H_2O \rightarrow 3.55Fe^{2+}Fe^{3+}{}_2O_{4\,(mgn)} + 9HS- + 5Ni^{2+} + 12.3\,H^+ + 3.55H_2$$

Both types of secondary magnetite formed during serpentinisation of these units, whereby serpentine-related fluids introduced aqueous Fe and removed S and Cu during the breakdown of olivine and sulphides (Li *et al.* 2004). Serpentine-related magnetite was too fine-grained to compositionally analyse, however, intercumulus sulphide-associated magnetite is Zr-Hf-V-Cr-poor and S-Cu-Ni-rich; a composition that is characteristic of secondary magnetite in sulphide ores (Duran *et al.* 2020).

6.5. The application of accessory minerals to magmatic sulphide exploration in the Labrador Trough

Resistance indicator minerals (RIMs) are becoming increasingly used in the exploration industry to vector towards exploration targets in vast and inaccessible regions (*e.g.,* Fennoscandia, Greenland, and Canada; Averill 2001; McClenaghan 2011; Gent *et al.* 2011; Duran *et al.* 2019). The Labrador Trough represents such a region, within which RIMs may be sourced from glacial, river, and lake deposits to assist in the delineation of several types of mineral deposits.

Regarding magmatic sulphide deposits, the halogen budget of apatite has been used to identify processes such as degassing and infiltration metasomatism (see Boudreau 2019). In the present study, Cl-poor fluorapatite (Cl/[Cl+F] < 0.2) occurs most mafic-ultramafic units regardless of sulphide content, whereas chlorapatite (Cl/[Cl+F] > 0.5) is exclusive to olivine cumulate units. While the lack of correlation between apatite Cl/(Cl+F) values and whole-rock PGE concentrations suggests that the presence of chloroapatite is not indicative of mineralised rocks, their presence is indicative of olivine cumulates, which are considered the most prospective rock type for magmatic sulphide mineralisation in the Labrador Trough (Clark & Wares 2005; Smith *et al.* 2020b).

Iron-titanium oxides, particularly magnetite, have been used as RIMs in the exploration for magmatic sulphides (Dupius & Beaudoin 2011; Boutroy *et al.* 2014; Nadoll *et al.* 2014; Ward *et al.* 2018). In the present study, we propose that sulphide-associated Cr-Ni-rich titanomagnetite and ilmenite formed during the interaction between sulphide-derived magnetite and Ti-bearing intercumulus melt, whereas sulphide-dissociated Fe-Ti oxides precipitated from fractionated silicate magma (Fig. 6A-B). Sulphide-associated titanomagnetite and ilmenite in this study have characteristically high Mg, Ni, and Cr concentrations, and are compositionally akin to those from ultramafic-hosted Ni-Cu-(PGE) sulphide occurrences worldwide (Fig. 6C-D; Dupius & Beaudoin 2011; Ward *et al.* 2018). The Ni/Cr values of

Fe-Ti oxides positively correlate with whole-rock PGE concentrations (see supplementary materials) suggesting that Fe-Ti oxides may be an effective RIM for magmatic sulphide occurrences in the Labrador Trough.

A key feature of optimal RIMs is their ability to retain primary compositions during post-magmatic erosion, transport, and deposition. While apatite may undergo dissolution during interaction with acidic meteoric waters (Morton & Hallsworth 1999), it has been shown that trace and halogen concentrations of detrital apatite will remain largely unaffected under surface conditions during diagenesis (Brenan 1994; Mao *et al.* 2016; Ansberque *et al.* 2019; O'Sullivan *et al.* 2020). The minor and trace element concentrations of magnetite, and by extension titanomagnetite and ilmenite, may be modified during hydrothermal re-equilibration (Hu *et al.* 2014; 2015). However, the concentrations of strongly compatible elements (*e.g.,* Cr, Ni, V; Donohue *et al.* 2012; Dare *et al.* 2014) remain unaffected by such processes, making them reliable provenance indicators (Dupius & Beaudoin 2011; Ward *et al.* 2018). One may use Figure 7 to categorise analysed *in situ* or detrital accessory minerals in the Labrador Trough, where those relating to the dark blue field are indicative of olivine cumulate units, and thus, prospective for magmatic sulphide mineralisation.

7. Conclusions

Apatite and Fe-Ti oxides are common accessory phases in mafic-ultramafic rocks of the Montagnais Sill Complex and their compositions are indicative of their host rock. Apatite grains contain variable F and OH concentrations and negligible Cl concentrations, regardless of the presence of spatially associated sulphides. Their composition is consistent with variable degrees of degassing and Cl-loss during Rayleigh fractionation and is not indicative of sulphide mineralisation. Intercumulus chlorapatite (Cl/[Cl+F] > 0.5) was identified only in mineralised olivine cumulate units at Huckleberry and thus, may be used to vector towards similar prospective rock types in the Labrador Trough.

Ilmenite is the dominant oxide in all mafic-ultramafic units, except for titanomagnetite in the titanomagnetite and granophyric gabbro units of the Huckleberry gabbro-peridotite sill. Magnetite occurred only as secondary magnetite in serpentinised olivine cumulates and is, therefore, not discriminative of sulphide mineralisation. Alteration and grain size prevented compositional analysis of Fe-Ti oxides in Idefix aphyric gabbro sills. Ilmenite and titanomagnetite in the mineralised olivine-bearing units have distinctly high Mg, Cr, Ni, Co, and Cu concentrations relative to those from other rock units and therefore, may be used to vector towards similar prospective rock units in the Labrador Trough. We believe that sulphide-associated ilmenite and titanomagnetite represent magnetite that has precipitated from evolved sulphide melts and subsequently interacted with FeO and TiO_2 in the co-existing silicate melt.

Acknowledgements

This work was published as part of W.D. Smith's PhD study, funded by the Natural Environment Research Council GW4+ doctoral training partnership (NE/L002434/1). Geologists at Northern Shield Resources are thanked for access to data, fieldwork, and sampling assistance. Mr. Anthony Oldroyd is thanked for making sample mounts and sections. The authors thank associate editor Erin Adlakha, David Good, and one anonymous reviewer for their kind and constructive reviews.

References

Ames, D.E., McClenaghan, M.B., Averill, S.A., and Milkereit, B. 2007. Footwall-hosted Cu-PGE (Au, Ag), Sudbury Canada: towards a new exploration vector. Exploration 07, Exploration in the New Millennium: 1013–1017.

Andersson, S.S., Wagner, T., Jonsson, E., Fusswinkel, T., and Whitehouse, M.J. 2019. Apatite as a tracer of the source, chemistry and evolution of ore-forming fluids: The case of the Olserum-Djupedal REE-phosphate mineralisation, SE Sweden. Geochimica et Cosmochimica Acta, 255: 163–187.

Ansberque, C., Mark, C., Caulfield, J.T., Chew, D.M., 2019. Combined in-situ determination of halogen (F, Cl) content in igneous and detrital apatite by SEM-EDS and LA-Q-ICPMS: A potential new provenance tool. Chem. Geol. 524, 406–420.

Armstrong, J.T. 1995. Citzaf-a package of correction programs for the quantitative Electron Microbeam X-Ray-Analysis of thick polished materials, thin-films, and particles. Microbeam Analysis, 4: 177–200.

Averill, S.A. 2001. The application of heavy indicator mineralogy in mineral exploration with emphasis on base metal indicators in glaciated metamorphic and plutonic terrains. Geological Society, London, Special Publications, 185: 69–81.

Baragar, W.R.A., Scoates, R.F.J., 1981. The Circum-Superior belt: a Proterozoic plate margin?, in: Developments in Precambrian Geology. Elsevier, pp. 297–330.

Belousova, E.A., Griffin, W.L., O'Reilly, S.Y., and Fisher, N.I. 2002. Apatite as an indicator mineral for mineral exploration: trace-element compositions and their relationship to host rock type. Journal of Geochemical Exploration, 76: 45–69.

Bosi, F., Hålenius, U., and Skogby, H. 2009. Crystal chemistry of the magnetite-ulvospinel series. American Mineralogist, 94: 181–189.

Boudreau, A.E. 2019. Hydromagmatic processes and platinum-group element deposits in layered intrusions. Cambridge University Press.

Boudreau, A.E., and Hoatson, D.M. 2004. Halogen variations in the Paleoproterozoic layered mafic-ultramafic intrusions of East Kimberley, Western Australia: Implications for platinum group element mineralization. Economic Geology, 99: 1015–1026.

Boudreau, A.E., and Hoatson, D.M. 2004. Halogen variations in the Paleoproterozoic layered mafic-ultramafic intrusions of East Kimberley, Western Australia: Implications for platinum group element mineralization. Economic Geology, 99: 1015–1026.

Boudreau, A.E., and McCallum, I.S. 1989. Investigations of the Stillwater Complex: Part V. Apatites as indicators of evolving fluid composition. Contributions to Mineralogy and Petrology, 102: 138–153.

Boudreau, A.E., and McCallum, I.S. 1992. Infiltration metasomatism in layered intrusions - An example from the Stillwater Complex, Montana. Journal of Volcanology and Geothermal Research, 52.

Boudreau, A.E., and Thompson, J.F.H. 1995. Fluid evolution in layered intrusions: evidence from the chemistry of the halogen-bearing minerals. Magmas, Fluids and Ore Deposits, 23: 25–46.

Boudreau, A.E., Love, C., and Prendergast, M.D. 1995. Halogen geochemistry of the Great Dyke, Zimbabwe. Contributions to Mineralogy and Petrology, 122: 289–300.

Boutroy, E., Dare, S.A.S., Beaudoin, G., Barnes, S.-J., and Lightfoot, P.C. 2014. Magnetite composition in Ni-Cu-PGE deposits worldwide: Application to mineral exploration. Journal of Geochemical Exploration, 145: 64–81.

Bouzari, F., Hart, C.J.R., Bissig, T., and Barker, S. 2016. Hydrothermal alteration revealed by apatite luminescence and chemistry: a potential indicator mineral for exploring covered porphyry copper deposits. Economic Geology, 111: 1397–1410.

Brenan, J., 1993. Kinetics of fluorine, chlorine and hydroxyl exchange in fluorapatite. Chem. Geol. 110, 195–210.

Broughm, S.G., Hanchar, J.M., Tornos, F., Westhues, A., and Attersley, S. 2017. Mineral chemistry of magnetite from magnetite-apatite mineralization and their host rocks: examples from Kiruna, Sweden, and El Laco, Chile. Mineralium Deposita, 52: 1223–1244.

Bruand, E., Fowler, M., Storey, C., and Darling, J.R. 2017. Apatite trace element and isotope applications to petrogenesis and provenance. American Mineralogist, 102: 75–84.

Bryson, S.E. 2017. A Geochemical Characterization of Streams Surrounding the Tom and Jason SEDEX Deposits of the MacMillan Pass, Yukon, Canada: Implications for Mineral Exploration and Toxicology. PhD Thesis University of Ottawa.

Buddington, A.F., and Lindsley, D.H. 1964. Iron-titanium oxide minerals and synthetic equivalents. Journal of petrology, 5: 310–357.

Chai, F., Yang, F., Liu, F., Santosh, M., Geng, X., Li, Q., and Liu, G. 2014. The Abagong apatite-rich magnetite deposit in the Chinese Altay Orogenic Belt: a Kiruna-type iron deposit. Ore Geology Reviews, 57: 482–497.

Chapman, R.J., Allan, M.M., Mortensen, J.K., Wrighton, T.M., and Grimshaw, M.R. 2018. A new indicator mineral methodology based on a generic Bi-Pb-Te-S mineral inclusion signature in detrital gold from porphyry and low/intermediate sulfidation epithermal environments in Yukon Territory, Canada. Mineralium Deposita, 53: 815–834.

Ciborowski, T.J.R., Minifie, M.J., Kerr, A.C., Ernst, R.E., Baragar, W.R.A., and Millar, I.L. 2017. A mantle plume origin for the Palaeoproterozoic Circum-Superior Large Igneous Province. Precambrian Research, 294: 189–213.

Clark, T. 1984. Géologie de la région,du lac Cambrien, Territoire du Nouveau Québec. Ministère des Ressources Naturelles du Québec Report number ET 83-02

Clark, T. 1989. Étude du gîte de Cu-Ni-Pd-Pt du lac Bleu no 1. Ministère des Ressources Naturelles du Québec Report number MB 89-35.

Clark, T. 1991. Le gîte no 1 du lac Bleu (Cu-Ni-Co-Pd-Pt). Ministère des Ressources Naturelles du Québec Report number MB 91-26.

Clark, T., and Wares, R.P. 2005. Lithotectonic and metallogenic synthesis of the New Quebec Orogen, Labrador Trough. Ministère des Ressources Naturelles du Québec Report number MM2005-01.

Coint, N., Keiding, J.K., Ihlen, P.M. 2020. Evidence for Silicate–Liquid Immiscibility in Monzonites and Petrogenesis of Associated Fe–Ti–P-rich rocks: Example from the Raftsund Intrusion, Lofoten, Northern Norway. Journal of Petrology 61:egaa045

Corrigan, D., Pehrsson, S.J., Wodicka, N., and De Kemp, E. 2009. The Palaeoproterozoic Trans-Hudson Orogen: a prototype of modern accretionary processes. Geological Society, London, Special Publications, 327: 457–479.

Corriveau, L., Ootes, L., Mumin, H., Jackson, V., Bennett, V., Cremer, J.F., Rivard, B., McMartin, I., Beaudoin, G., and Milkereit, B. 2007. Alteration vectoring to IOCG (U) deposits in frontier volcano-plutonic terrains, Canada. In Proceedings of exploration. pp. 1171–1177.

Dare, S.A.S., Barnes, S.-J., and Beaudoin, G. 2012. Variation in trace element content of magnetite crystallized from a fractionating sulfide liquid, Sudbury, Canada: Implications for provenance discrimination. Geochimica et Cosmochimica Acta, 88: 27–50.

Dare, S.A.S., Barnes, S.-J., Beaudoin, G., Méric, J., Boutroy, E., and Potvin-Doucet, C. 2014. Trace elements in magnetite as petrogenetic indicators. Mineralium Deposita, 49: 785–796.

Das, K., Tomioka, N., Bose, S., Ando, J., Ohnishi, I., 2017. The occurrence of fluor-wagnerite in UHT granulites and its implications towards understanding fluid regimes in the evolution of deep crust: a case study from the Eastern Ghats Belt, India. Mineral. Petrol. 111, 417–429.

Deer, W.A., Howie, R.A., and Zussman, J. 1992. An introduction to the rock-forming minerals. In 2nd edition. Pearson Education Ltd.

Donohue, P.H., Simonetti, A., Neal, C.R., 2012. Chemical characterisation of natural ilmenite: A possible new reference material. Geostand. Geoanalytical Res. 36, 61–73.

Drinkwater, J.L., Czamanske, G.K., and Ford, A.B. 1990. Apatite of the Dufek intrusion: distribution, paragenesis, and chemistry. Canadian Mineralogist, 28: 835–854.

Dupuis, C., and Beaudoin, G. 2011. Discriminant diagrams for iron oxide trace element fingerprinting of mineral deposit types. Mineralium Deposita, 46: 319–335.

Duran, C.J., Barnes, S.-J., and Corkery, J.T. 2016. Trace element distribution in primary sulfides and Fe – Ti oxides from the sulfide-rich pods of the Lac des Iles Pd deposits, Western Ontario, Canada: Constraints on processes controlling the composition of the ore and the use of pentlandite compos. Journal of Geochemical Exploration, 166: 45–63.

Duran, C.J., Barnes, S.-J., Mansur, E.T., Dare, S.A.S., Bédard, L.P., and Sluzhenikin, S.F. 2020. Magnetite chemistry by LA-ICP-MS records sulfide fractional crystallization in massive nickel-copper-platinum group element ores from the Norilsk-Talnakh mining district (Siberia, Russia): Implications for trace element partitioning into magnetite. Economic Geology, 115: 1245–1266.

Duran, C.J., Dubé-Loubert, H., Pagé, P., Barnes, S.-J., Roy, M., Savard, D., Cave, B.J., Arguin, J.-P., and Mansur, E.T. 2019. Applications of trace element chemistry of pyrite and chalcopyrite in glacial sediments to mineral exploration targeting: Example from the Churchill Province, northern Quebec, Canada. Journal of Geochemical Exploration, 196: 105–130.

Findlay, J.M., Parrish, R.R., Birkett, T.C., and Watanabe, D.H. 1995. U Pb ages from the Nimish Formation and Montagnais glomeroporphyritic gabbro of the central New Quebec Orogen, Canada1. 1220: 1208–1220.

Gál, B., Molnár, F., Guzmics, T., Mogessie, A., Szabó, C., and Peterson, D.M. 2013. Segregation of magmatic fluids and their potential in the mobilization of platinum-group elements in the South Kawishiwi intrusion, Duluth Complex, Minnesota—evidence from petrography, apatite geochemistry and coexisting fluid and melt inclusions. Ore Geology Reviews, 54: 59–80.

Gent, M., Menendez, M., Toraño, J., and Torno, S. 2011. A review of indicator minerals and sample processing methods for geochemical exploration. Journal of Geochemical Exploration, 110: 47–60.

Girard, R., and Gagnon, P. 2005. Rapport de Travaux de Terrain, Project de Romer. IOS Services Géoscientifiques Inc. Ministère des Ressources Naturelles du Québec Report number GM 61887.

Goldoff, B., Webster, J.D., Harlov, D.E., 2012. Characterization of fluor-chlorapatites by electron probe microanalysis with a focus on time-dependent intensity variation of halogens. Am. Mineral. 97, 1103–1115.

Harlov, D.E. 2015. Apatite: a fingerprint for metasomatic processes. Elements, 11: 171–176.

Henrique-Pinto, R., Guilmette, C., Bilodeau, C., Stevenson, R., and Carvalho, B.B. 2019. Petrography, geochemistry, and Nd isotope systematics of metaconglomerates and matrix-rich metasedimentary rocks: implications for the provenance and tectonic setting of the Labrador Trough, Canada. Canadian Journal of Earth Sciences, 56: 672–687.

Hoffman, P.F. 1990. Dynamics of the tectonic assembly of the northeast Laurentia in geon 18 (1.9-1.8 Ga). Geoscience Canada, 17: 222–226.

Hu, H., Lentz, D., Li, J.-W., McCarron, T., Zhao, X.-F., Hall, D., 2015. Reequilibration processes in magnetite from iron skarn deposits. Econ. Geol. 110, 1–8.

Hu, H., Li, J.-W., Lentz, D., Ren, Z., Zhao, X.-F., Deng, X.-D., Hall, D., 2014. Dissolution–reprecipitation process of magnetite from the Chengchao iron deposit: insights into ore genesis and implication for in-situ chemical analysis of magnetite. Ore Geol. Rev. 57, 393–405.

Hughes, J.M., and Rakovan, J.F. 2015. Structurally robust, chemically diverse: apatite and apatite supergroup minerals. Elements, 11: 165–170.

Jaques, A.L. 1976. An archean tholeiitic layered sill from Mt Kilkenny, Western Australia. Journal of the Geological Society of Australia, 23: 157–168.

Jochum, K.P., Nohl, U., Herwig, K., Lammel, E., Stoll, B., and Hofmann, A.W. 2005. GeoReM: a new geochemical database for reference materials and isotopic standards. Geostandards and Geoanalytical Research, 29: 333–338.

Kaminsky, F.V., and Belousova, E.A. 2009. Manganoan ilmenite as kimberlite/diamond indicator mineral. Russian Geology and Geophysics, 50: 1212–1220.

Karinen, T.T., Hanski, E.J., and Taipale, A. 2015. The Mustavaara Fe-Ti-V oxide deposit. In Mineral deposits of Finland. 179–194.

Kastek, N., Mungall, J.E., Ernst, R.E., and Cousens, B.L. 2020. Roberts Lake Syncline mafic lavas (NE Superior craton): A proposed extension of the Cape Smith belt. Lithos: 105545.

Klemm, D.D., Snethlage, R., Dehm, R.M., Henckel, J., and Schmidt-Thome, R. 1982. The formation of chromite and titanomagnetite deposits within the Bushveld Igneous Complex. In Ore Genesis. Springer. pp. 351–370.

Konecke, B. 2019. Sulfur in Apatite as a Volatile and Redox Tracer in Magmatic and Magmatic-Hydrothermal Systems. PhD Thesis University of Michigan

La Cruz, N.L. 2019. Using the Geochemistry of Magnetite and Apatite to Gain Insights Into the Genesis of Kiruna-type Ore Deposits and for Exploration in Densely Covered Terrains. PhD Thesis University of Michigan

Lacroix, S., and Darling, R. 1991. Tectonized Cu-Ni Deposits of the Aulneau-Redcliff Area, Central Labrador Trough, Quebec. Economic Geology, 86: 718–739.

Laurent, R. 1995. Petrologie des filons-couches gabbroiques mineralises de la region du lac Bleu. Ministère des Ressources Naturelles du Québec Report number ET 93-04.

Layton-Matthews, D., Hamilton, C., and McClenaghan, M.B. 2014. Mineral chemistry: modern techniques and applications to exploration. Application of Indicator Mineral Methods to Mineral Exploration (ed.) MB McClenaghan, A. Plouffe, and D. Layton-Matthews: 9–18.

Li, C., Ripley, E.M., Merino, E., and Maier, W.D. 2004. Replacement of base metal sulfides by actinolite, epidote, calcite, and magnetite in the UG2 and Merensky Reef of the Bushveld Complex, South Africa. Economic Geology, 99: 173–184.

Liang, X., Zhong, Y., Zhu, S., He, H., Yuan, P., Zhu, J., and Jiang, Z. 2013. The valence and site occupancy of substituting metals in magnetite spinel structure Fe3− xMxO4 (M= Cr, Mn, Co and Ni) and their influence on thermal stability: An XANES and TG-DSC investigation. Solid state sciences, 15: 115–122.

Liu, M.-Y., Zhou, M.-F., Su, S.-G., and Chen, X.-G. 2021. Contrasting Geochemistry of Apatite from Peridotites and Sulfide Ores of the Jinchuan Ni-Cu Sulfide Deposit, NW China. Economic Geology, 116: 1073–1092.

Lypaczewski, P., Normandeau, P.X., Paquette, J., and McMartin, I. 2013. Petrographic and cathodoluminescence characterization of apatite from the Sue-Dianne and Brooke IOCG mineralization systems, Great Bear magmatic zone, Northwest Territories, Canada. Geol Surv Can, Open File, 7319.

Machado, N., Clark, T., David, J., and Goulet, N. 1997. U-Pb ages for magmatism and deformation in the new Quebec Orogen. Canadian Journal of Earth Sciences, 34: 716–723.

Maes, S.M., Tikoff, B., Ferré, E.C., Brown, P.E., and Miller Jr, J.D. 2007. The Sonju Lake layered intrusion, northeast Minnesota: Internal structure and emplacement history inferred from magnetic fabrics. Precambrian Research, 157: 269–288.

Makvandi, S., Beaudoin, G., McClenaghan, M.B., and Layton-Matthews, D. 2015. The surface texture and morphology of magnetite from the Izok Lake volcanogenic massive sulfide deposit and local glacial sediments, Nunavut, Canada: Application to mineral exploration. Journal of Geochemical Exploration, 150: 84–103.

Makvandi, S., Beaudoin, G., McClenaghan, M.B., and Quirt, D. 2017. Geochemistry of magnetite and hematite from unmineralized bedrock and local till at the Kiggavik uranium deposit: Implications for sediment provenance. Journal of Geochemical Exploration, 183: 1–21.

Makvandi, S., Ghasemzadeh-Barvarz, M., Beaudoin, G., Grunsky, E.C., McClenaghan, M.B., Duchesne, J.-C., and Boutroy, E. 2016. Partial least squares-discriminant analysis of trace element compositions of magnetite from various VMS deposit subtypes: Application to mineral exploration. Ore Geology Reviews, 78: 388–408.

Mao, M., Rukhlov, A.S., Rowins, S.M., Spence, J., and Coogan, L.A. 2016. Apatite trace element compositions: a robust new tool for mineral exploration. Economic Geology, 111: 1187–1222.

Mathez, E.A., and Webster, J.D. 2005. Partitioning behavior of chlorine and fluorine in the system apatite-silicate melt-fluid. Geochimica et Cosmochimica Acta, 69: 1275–1286.

Mathieu, L. 2019. Origin of the Vanadiferous Serpentine–Magnetite Rocks of the Mt. Sorcerer Area, Lac Doré Layered Intrusion, Chibougamau, Québec. Geosciences, 9: 110.

McBirney, A.R. 1980. Mixing and unmixing of magmas. Journal of Volcanology and Geothermal Research, 7: 357–371.

McBirney, A.R., and Sonnenthal, E.L. 1990. Metasomatic replacement in the Skaergaard Intrusion, East Greenland: preliminary observations. Chemical Geology, 88: 245–260.

McClenaghan, M.B. 2011. Overview of common processing methods for recovery of indicator minerals from sediment and bedrock in mineral exploration. AAG/Geological Society of London.

McClenaghan, M.B., Kjarsgaard, B.A., and Goodfellow, W.D. 2007. Indicator mineral and surficial geochemical exploration methods for kimberlite in glaciated terrain, examples from Canada. Mineral Resources of Canada: A Synthesis of Major Deposit-types, District Metallogeny, the Evolution of Geological Provinces and Exploration Methods. Geological Association of Canada, Special Publication, 4: 1998.

McQueen, K.G., and Cross, A.J. 1998. Magnetite as a geochemical sampling medium: application to skarn deposits. Brisbane, Geological Society of Australia: 194–199.

Méric, J. 2011. Caractérisation géochimiques des magnétites de la zone critique de l’intrusion magmatique de Sept-Iles (Québec, Canada) et intégration a une base de données utilisant la signature géochimique des oxydes de fer comme outil d’exploration. MSc Thesis Université du Québec à Chicoutimi.

Meurer, W.P., Hellström, F.A., and Claeson, D.T. 2004. The relationship between chlorapatite and PGE-rich cumulates in layered intrusions: The Kläppsjö Gabbro, north-central Sweden, as a case study. Canadian Mineralogist, 42: 279–289.

Morton, A.C., Hallsworth, C.R., 1999. Processes controlling the composition of heavy mineral assemblages in sandstones. Sediment. Geol. 124, 3–29.

Mungall, J.E. 1998. Final report on the 1998 reconnaissance program, Payne Bay property. Ministère des Ressources Naturelles du Québec Report number GM 56799

Mutanen, T. 1997. Geology and ore petrology of the Akanvaara and Koitelainen mafic layered intrusions and the Keivitsa-Satovaara layered complex, northern Finland. In Bulletin Geological Survey of Finland.

Nadoll, P., Angerer, T., Mauk, J.L., French, D., and Walshe, J. 2014. The chemistry of hydrothermal magnetite: a review. Ore Geology Reviews, 61: 1–32.

Nadoll, P., Mauk, J.L., Leveille, R.A., and Koenig, A.E. 2015. Geochemistry of magnetite from porphyry Cu and skarn deposits in the southwestern United States. Mineralium Deposita, 50: 493–515.

Naldrett, A.J. 1969. A Portion of the System Fe–S–O between 900 and 1080 °C and its Application to Sulfide Ore Magmas. Journal of Petrology, 10: 171–201.

Namur, O., Charlier, B., and Holness, M.B. 2012. Dual origin of Fe-Ti-P gabbros by immiscibility and fractional crystallization of evolved tholeiitic basalts in the Sept Iles layered intrusion. Lithos, 154: 100–114.

Naslund, H.R. 1989. Petrology of the Basistoppen Sill, East Greenland: a calculated magma differentiation trend. Journal of Petrology, 30: 299–319.

Néron, A. 2011. Caractérisation géochimique des oxydes de Fe-Ti dans un dépôt de Fe-Ti-P associé à la suite anorthositique du Lac-Saint-Jean, Québec, Canada secteur Lac à Paul et intégration des données du secteur Lac à la Mine. MSc thesis University of Quebec at Chicoutimi.

O'Sullivan, G., Chew, D., Kenny, G., Henrichs, I., and Mulligan, D. 2020. The trace element composition of apatite and its application to detrital provenance studies. Earth-Science Reviews, 201: 103044.

Pang, K.-N., Zhou, M.-F., Lindsley, D.H., Zhao, D.M., and Malpas, J. 2008. Origin of Fe–Ti oxide ores in mafic intrusions: evidence from the Panzhihua intrusion, SW China. Journal of Petrology, 49: 295–313.

Pasero, M., Kampf, A.R., Ferraris, C., Pekov, I.V., Rakovan, J.F., and White, T.J. 2010. Nomenclature of the apatite supergroup minerals. European Journal of Mineralogy, 22: 163–179.

Pisiak, L.K., Canil, D., Grondahl, C., Plouffe, A., Ferbey, T., and Anderson, R.G. 2014. Magnetite as a porphyry copper indicator mineral in till: A test using the Mount Polley porphyry copper-gold deposit, south-central British Columbia (NTS 093A). Geoscience BC Summary of Activities: 2011–2015.

Pisiak, L.K., Canil, D., Lacourse, T., Plouffe, A., and Ferbey, T. 2017. Magnetite as an indicator mineral in the exploration of porphyry deposits: a case study in till near the Mount Polley Cu-Au deposit, British Columbia, Canada. Economic Geology, 112: 919–940.

Prichard, H.M., Hutchinson, D., and Fisher, P.C. 2004. Petrology and crystallization history of multiphase sulfide droplets in a mafic dike from Uruguay: implications for the origin of Cu-Ni-PGE sulfide deposits. Economic Geology, 99: 365–376.

Raič, S., Mogessie, A., Krenn, K., Hauzenberger, C.A., and Tropper, P. 2018. Deciphering Magmatic and Metasomatic Processes Recorded by Fluid Inclusions and Apatite within the Cu–Ni±PGE-Sulfide Mineralized Bathtub Intrusion of the Duluth Complex, NE Minnesota, USA. Journal of Petrology, 59: 1167–1192.

Reynolds, I.M. 1985. The nature and origin of titaniferous magnetite-rich layers in the upper zone of the Bushveld Complex; a review and synthesis. Economic Geology, 80: 1089–1108.

Rudnick, R.L., and Gao, S. 2003. Composition of the Continental Crust. Treatise on geochemistry, 3: 659.

Sauerzapf, U., Lattard, D., Burchard, M., and Engelmann, R. 2008. The titanomagnetite–ilmenite equilibrium: new experimental data and thermo-oxybarometric application to the crystallization of basic to intermediate rocks. Journal of Petrology, 49: 1161–1185.

Schisa, P., Boudreau, A.E., Djon, M.-L., Tchalikian, A., and Corkery, J.T. 2015. The Lac Des Iles Palladium Deposit, Ontario, Canada. Part II. Halogen variations in apatite. Mineralium Deposita, 50: 339–355.

Sievwright, R.H. 2017. Developing magnetite chemistry as an exploration tool for porphyry copper deposits. PhD Thesis Imperial College London.

Simandl, G.J., Mackay, D.A.R., Ma, X., Luck, P., Gravel, J., and Akam, C. 2017. The direct indicator mineral concept and QEMSCAN® applied to exploration for carbonatite and carbonatite-related ore deposits. Indicator minerals in till and stream sediments of the Canadian cordillera. Geological Association of Canada Special Paper, 50: 175–190.

Smith, W.D., Maier, W.D., and Bliss, I. 2020a. Contact-style magmatic sulphide mineralisation in the Labrador trough, northern Quebec, Canada: Implications for regional prospectivity. Canadian Journal of Earth Sciences, 57: 867–883.

Smith, W.D., Maier, W.D., and Bliss, I. 2020b. The geology, geochemistry, and petrogenesis of the Huckleberry Cu-Ni-PGE prospect in the Labrador Trough, Canada: Perspectives for regional prospectivity. Ore Geology Reviews: 103905.

Smith, W.D., Maier, W.D., Bliss, I., and Martin, L.A.J. 2021a. In situ multiple sulfur isotope and S/Se composition of magmatic sulfide occurrences in the Labrador Trough, northern Québec. Economic Geology.

Smith, W.D., Maier, W.D., and Bliss, I. 2021b. Distribution of noble metals in magmatic sulfide occurrences in the Montagnais Sill Complex, Labrador Trough, Canada. Canadian Mineralogist 59 (6): 1599–1626.

Stock, M.J., Humphreys, M.C.S., Smith, V.C., Johnson, R.D., Pyle, D.M., EIMF, 2015. New constraints on electron-beam induced halogen migration in apatite. Am. Mineral. 100, 281–293.

Stormer, J.C., Pierson, M.L., Tacker, R.C., 1993. Variation of F and Cl X-ray intensity due to anisotropic diffusion in apatite during electron microprobe analysis. Am. Mineral. 78, 641–648.

Tan, W., Wang, C.Y., He, H., Xing, C.M., Liang, X., and Dong, H. 2015. Magnetite-rutile symplectite derived from ilmenite-hematite solid solution in the Xinjie Fe-Ti oxide-bearing, mafic-ultramafic layered intrusion (SW China). American Mineralogist, 100: 2348–2351.

Vaillancourt, C., and Murray, G. 2017. Report on the Huckleberry property: surface sampling, mapping and drilling program 2016. Northern Shield Resources. Ministère des Ressources Naturelles du Québec Report number GM 70593.

Vaillancourt, C., Simard, R.-L., Bliss, I., Babineau, J., Budulan, G., and Sharman, E.R. 2012. Report on the Idefix property and reconnaissance in the northern Labrador Trough - programs 2011-2012. Ministère des Ressources Naturelles du Québec Report number GM 67894.

Van Kan Parker, M., Mason, P.R.D., and Van Westrenen, W. 2011. Trace element partitioning between ilmenite, armalcolite and anhydrous silicate melt: Implications for the formation of lunar high-Ti mare basalts. Geochimica et Cosmochimica Acta, 75: 4179–4193.

Veksler, I. V, and Charlier, B. 2015. Silicate liquid immiscibility in layered intrusions. In Layered intrusions. Springer. pp. 229–258.

Wager, L.R. 1960. The major element variation of the layered series of the Skaergaard intrusion and a re-estimation of the average composition of the hidden layered series and of the successive residual magmas. Journal of Petrology, 1: 364–398.

Wager, L.R., and Brown, G.M. 1968. Layered igneous intrusions. Edinburgh and London: Oliver and Boyd: 1–588.

Ward, L.A., Holwell, D.A., Barry, T.L., Blanks, D.E., and Graham, S.D. 2018. The use of magnetite as a geochemical indicator in the exploration for magmatic Ni-Cu-PGE sulfide deposits: A case study from Munali, Zambia. Journal of Geochemical Exploration, 188: 172–184.

Wardle, R.J., and Van Kranendonk, M.J. 1996. The Palaeoproterozoic Southeastern Churchill Province of Labrador-Quebec, Canada: orogenic development as a consequence of oblique collision and indentation. Precambrian Crustal Evolution in the North Atlantic Region, 112: 137–153.

Wares, R.P., and Mungall, J.E. 1997. Final report on the 1996 exploration program, Hawk Ridge property. Ministère des Ressources Naturelles du Québec Report number GM 54913

Willmore, C.C., Boudreau, A.E., and Kruger, F.J. 2000. The halogen geochemistry of the Bushveld Complex, Republic of South Africa: implications for chalcophile element distribution in the lower and critical zones. Journal of petrology, 41: 1517–1539.

Wilson, N.C., Muscat, J., Mkhonto, D., Ngoepe, P.E., and Harrison, N.M. 2005. Structure and properties of ilmenite from first principles. Physical Review B, 71: 75202.

Wyatt, B.A., Baumgartner, M., Anckar, E., and Grutter, H. 2004. Compositional classification of “kimberlitic” and “non-kimberlitic” ilmenite. Lithos, 77: 819–840.

Figure captions

Figure 1. A. QGIS3.4 map of the Labrador Trough showing the aerial extent of intrusive and extrusive rocks of the Montagnais Sill Complex as well as the Baby and Menihek metasedimentary formations. The symbols represent magmatic, magmatic-hydrothermal, and exhalative sulphide occurrences sourced from the SIGÉOM database of the Ministère des Ressources Naturelles du Québec. The inset map shows the location of the Labrador Trough in Canada. **B-C.** Schematic cross-section of the Idefix PGE-Cu (B) and Huckleberry Cu-Ni-(PGE) (C) prospects showing the rock units and stratigraphic occurrence of sulphide mineralization (modified from Smith *et al.* 2020a; Smith 2020b).

Figure 2. SEM-EDS element maps showing the distribution of apatite and Fe-Ti oxides in mafic-ultramafic rocks of this study. **A.** Globular sulphides in aphyric gabbro at Idefix (ID11-70). **B.** Disseminated sulphides in aphyric gabbro at Idefix (ID06B). **C.** Globular sulphides in the PGU at Huckleberry (HK08-415). Note how Fe-Ti oxides partially rim the sulphide globule and are disseminated around the globule together with sulphides. **D.** Net-textured sulphides in the basal olivine cumulate unit at Huckleberry (HK07-119). Note the inset map of an intercumulus apatite grain with a Cl-rich core. **E.** Net-textured sulphides in the footwall olivine cumulate unit at Huckleberry. Note the titanomagnetite-ilmenite intergrowths at the silicate-sulphide grain boundary and the magnetite stringers. **F.** Sparsely mineralised titanomagnetite gabbro at Huckleberry. Note this unit is dominated by titanomagnetite with ilmenite exsolution lamellae. **G**. Granophyric gabbro unit at Huckleberry. Note the clusters of intercumulus apatite at the margins of altered Fe-Ti oxide grains. Mineral abbreviations: amp = amphibole, ap = apatite, cbn = cubanite, ccp = chalcopyrite, ilm = ilmenite, mgn = magnetite, ox = Fe-Ti oxides, pn = pentlandite, po = pyrrhotite, sul = sulphides, tmg = titanomagnetite, ttn = titanite.

Figure 3. A. F-Cl-OH ternary diagram showing 95th percentile contours of apatite measured from the three sill types analysed in this study. Typical compositional trends of apatite from its equilibrated composition are from Schisa *et al.* (2015). **B.** F-Cl-OH ternary diagram showing all apatite measured in this study underlain with compositional fields of apatite from Skaergaard (Boudreau & McCallum 1989), Munni Munni (Boudreau & Hoatson 2004), Kläppsjö (Meurer *et al.* 2004), the Stillwater and Bushveld reefs (Boudreau *et al.* 1986), Windimurra (Boudreau & Thompson 1995), Duluth (Gál *et al.* 2013), Dufek (Drinkwater *et al.* 1990), Great Dyke (Boudreau *et al.* 1995), and Jinchuan (Liu *et al.* 2021). Note the division of apatite present in olivine cumulate units compared with the rest of the dataset.

Figure 4. Reflected light photomicrographs showing the texture of Fe-Ti oxides. **A.** Titanite replacing ilmenite amongst globular sulphides at Idefix (ID13-204). **B**. Titanite replacing ilmenite amongst disseminated sulphides at Idefix (ID06B). **C.** Subhedral ilmenite amongst globular sulphides in the PGU at Huckleberry (HK02C). **D.** Anhedral ilmenite amongst disseminated sulphides in the glomeroporphyritic gabbro unit at Huckleberry (HK0024). **E-F.** Ilmenite and titanomagnetite amongst

net-textured sulphides in the basal olivine cumulate unit at Huckleberry (HK08-317a and HK07-119). **G-I.** Anhedral magnetite amongst net-textured sulphides in the footwall olivine cumulate units at Huckleberry (HK12-554b). **J.** Titanomagnetite-ilmenite intergrowths in the titanomagnetite gabbro at Huckleberry (HK09-197). **K.** Titanomagnetite-ilmenite intergrowths in granophyric gabbro at Huckleberry (HK09-227). **L.** Magnetite and chalcopyrite intergrowths in the footwall olivine cumulate unit at Huckleberry (HK1024a). Mineral abbreviations: ars = sulpharsenides, cbn = cubanite, ccp = chalcopyrite, ilm = ilmenite, mgn = magnetite, pn = pentlandite, po = pyrrhotite, tmg = titanomagnetite, ttn = titanite.

Figure 5. Multi-element diagrams of ilmenite (A-D) and titanomagnetite and magnetite (E-F). The elements are ordered by increasing compatibility into magnetite (see Dare *et al.* 2012) and normalised to the bulk continental crust (Rudnick & Gao 2003). The grey lines represent detection limits.

Figure 6. A-B. Cr *versus* V and Ni for Fe-Ti oxides. Stippled fields represent the compositional fields of Fe-Ti oxides exsolved from evolving sulphide melts (Dare *et al.* 2014). Red dashed lines correspond to detection limits. **C.** Si+Mg *versus* Ni+Cr deposit type discrimination diagram of Dupius & Beaudoin (2011). **D.** Cr/V *versus* Ni exploration discrimination diagram of Ward *et al.* (2018). Note how Fe-Ti oxides are most consistent with those derived from evolved *mss* and that titanomagnetite hosted in the ultramafic cumulates units are consistent with those derived from ultramafic-hosted Ni-Cu-(PGE) sulphide deposits.

Figure 7. A. F-Cl-OH apatite ternary diagram with 95th percentile contours for apatite grains present in aphyric gabbro sills (light blue field), glomeroporphyritic gabbros (green field), titanomagnetite and granophyric gabbros (yellow field), and olivine cumulate units (dark blue field). Note that apatite grains indicating potential economic interest plot in the dark blue field. **B.** Cr *versus* Ni discrimination diagram for titanomagnetite and ilmenite in the Labrador Trough. **C.** Cr/V *versus* Ni discrimination diagram for titanomagnetite and ilmenite in the Labrador Trough (modified from Ward *et al.* 2018). Those that plot in the dark blue field are considered a good indication of proximal mineralised olivine cumulate units in the Labrador Trough

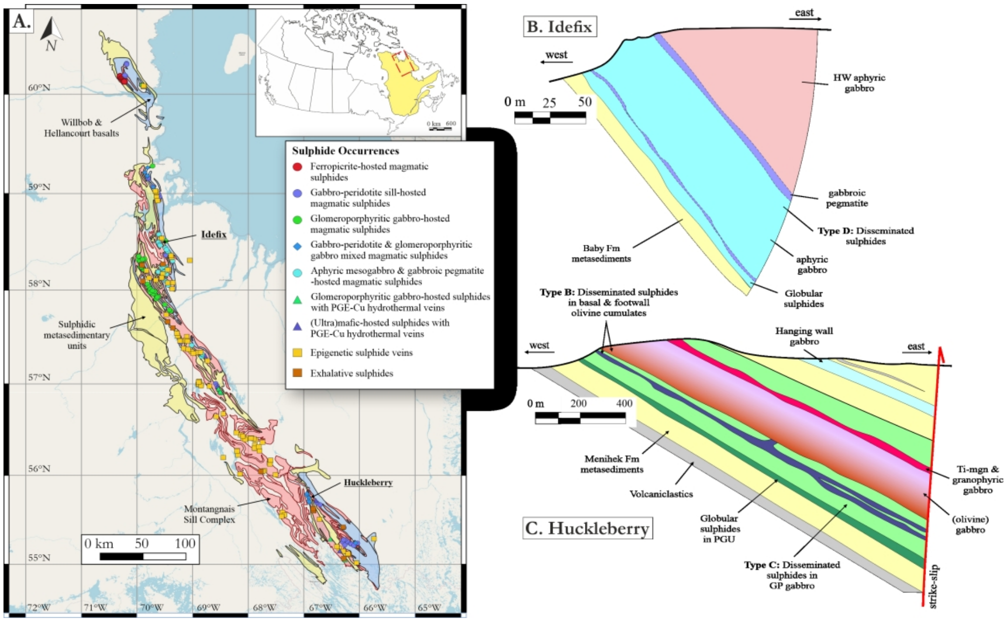

Figure 1. A. QGIS3.4 map of the Labrador Trough showing the aerial extent of intrusive and extrusive rocks of the Montagnais Sill Complex as well as the Baby and Menihek metasedimentary formations. The symbols represent magmatic, magmatic-hydrothermal, and exhalative sulphide occurrences sourced from the SIGÉOM database of the Ministère des Ressources Naturelles du Québec. The inset map shows the location of the Labrador Trough in Canada. B-C. Schematic cross-section of the Idefix PGE-Cu (B) and Huckleberry Cu-Ni-(PGE) (C) prospects showing the rock units and stratigraphic occurrence of sulphide mineralization (modified from Smith et al. 2020a; Smith 2020b).

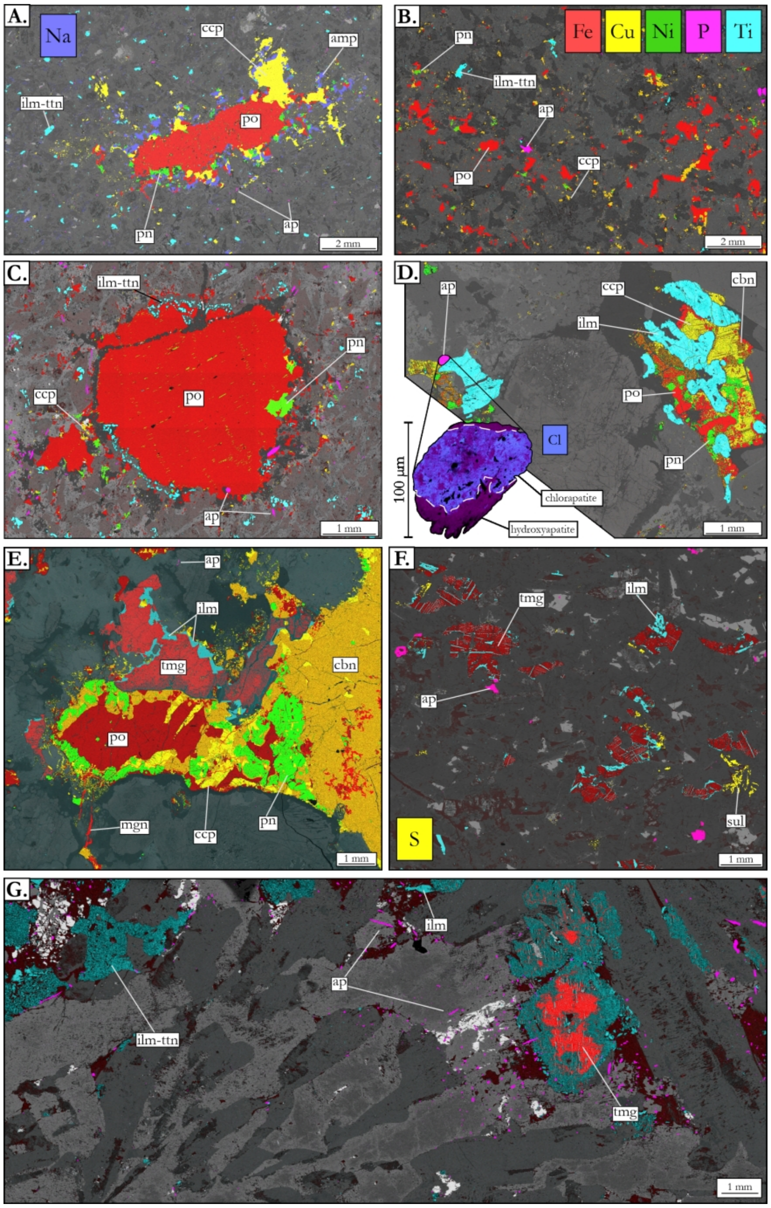

Figure 2. SEM-EDS element maps showing the distribution of apatite and Fe-Ti oxides in mafic-ultramafic rocks of this study. A. Globular sulphides in aphyric gabbro at Idefix (ID11-70). B. Disseminated sulphides in aphyric gabbro at Idefix (ID06B). C. Globular sulphides in the PGU at Huckleberry (HK08-415). Note how Fe-Ti oxides partially rim the sulphide globule and are disseminated around the globule together with sulphides. D. Net-textured sulphides in the basal olivine cumulate unit at Huckleberry (HK07-119). Note the inset map of an intercumulus apatite grain with a Cl-rich core. E. Net-textured sulphides in the footwall olivine cumulate unit at Huckleberry. Note the titanomagnetite-ilmenite intergrowths at the silicate-sulphide grain boundary and the magnetite stringers. F. Sparsely mineralised titanomagnetite gabbro at Huckleberry. Note this unit is dominated by titanomagnetite with ilmenite exsolution lamellae. G. Granophyric gabbro unit at Huckleberry. Note the clusters of intercumulus apatite at the margins of altered Fe-Ti oxide grains. Mineral abbreviations: amp = amphibole, ap = apatite, cbn = cubanite, ccp = chalcopyrite, ilm = ilmenite, mgn = magnetite, ox = Fe-Ti oxides, pn = pentlandite, po = pyrrhotite, sul = sulphides, tmg = titanomagnetite, ttn = titanite.

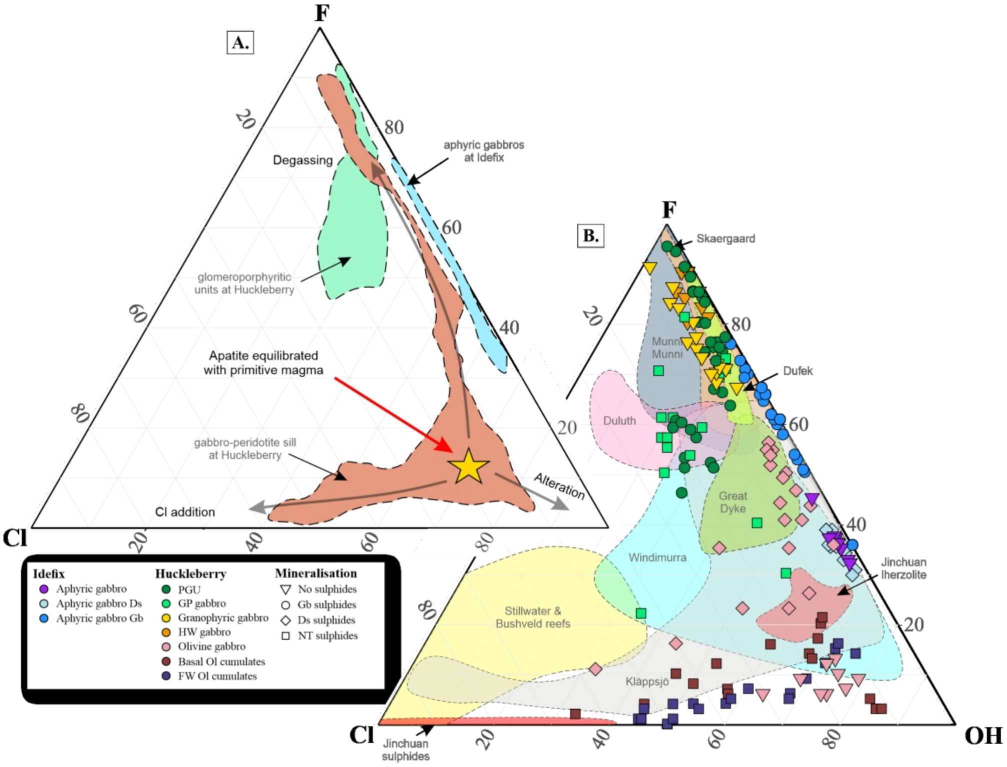

Figure 3. A. F-Cl-OH ternary diagram showing 95th percentile contours of apatite measured from the three sill types analysed in this study. Typical compositional trends of apatite from its equilibrated composition are from Schisa et al. (2015). B. F-Cl-OH ternary diagram showing all apatite measured in this study underlain with compositional fields of apatite from Skaergaard (Boudreau & McCallum 1989), Munni Munni (Boudreau & Hoatson 2004), Kläppsjö (Meurer et al. 2004), the Stillwater and Bushveld reefs (Boudreau et al. 1986), Windimurra (Boudreau & Thompson 1995), Duluth (Gál et al. 2013), Dufek (Drinkwater et al. 1990), Great Dyke (Boudreau et al. 1995), and Jinchuan (Liu et al. 2021). Note the division of apatite present in olivine cumulate units compared with the rest of the dataset.

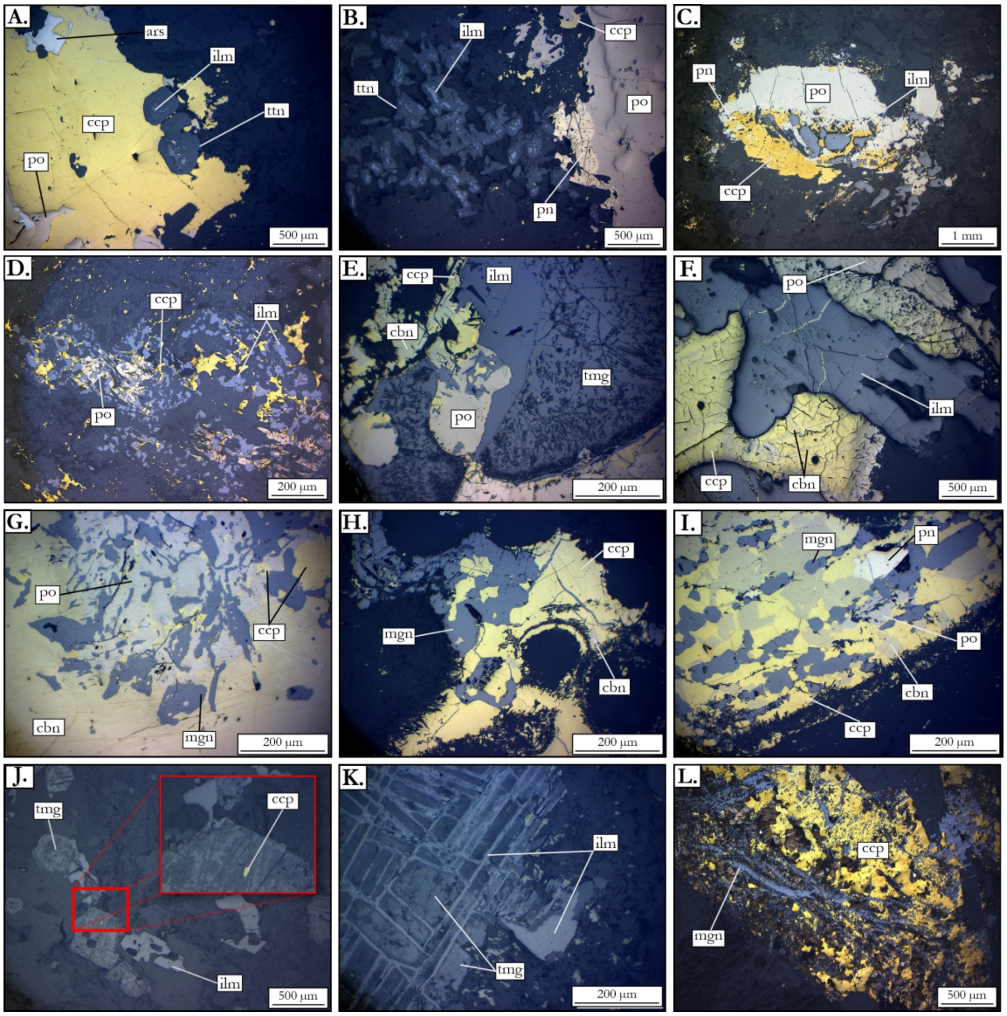

Figure 4. Reflected light photomicrographs showing the texture of Fe-Ti oxides. A. Titanite replacing ilmenite amongst globular sulphides at Idefix (ID13-204). B. Titanite replacing ilmenite amongst disseminated sulphides at Idefix (ID06B). C. Subhedral ilmenite amongst globular sulphides in the PGU at Huckleberry (HK02C). D. Anhedral ilmenite amongst disseminated sulphides in the glomeroporphyritic gabbro unit at Huckleberry (HK0024). E-F. Ilmenite and titanomagnetite amongst net-textured sulphides in the basal olivine cumulate unit at Huckleberry (HK08-317a and HK07-119). G-I. Anhedral magnetite amongst net-textured sulphides in the footwall olivine cumulate units at Huckleberry (HK12-554b). J. Titanomagnetite-ilmenite intergrowths in the titanomagnetite gabbro at Huckleberry (HK09-197). K. Titanomagnetite-ilmenite intergrowths in granophyric gabbro at Huckleberry (HK09-227). L. Magnetite and chalcopyrite intergrowths in the footwall olivine cumulate unit at Huckleberry (HK1024a). Mineral abbreviations: ars = sulpharsenides, cbn = cubanite, ccp = chalcopyrite, ilm = ilmenite, mgn = magnetite, pn = pentlandite, po = pyrrhotite, tmg = titanomagnetite, ttn = titanite.

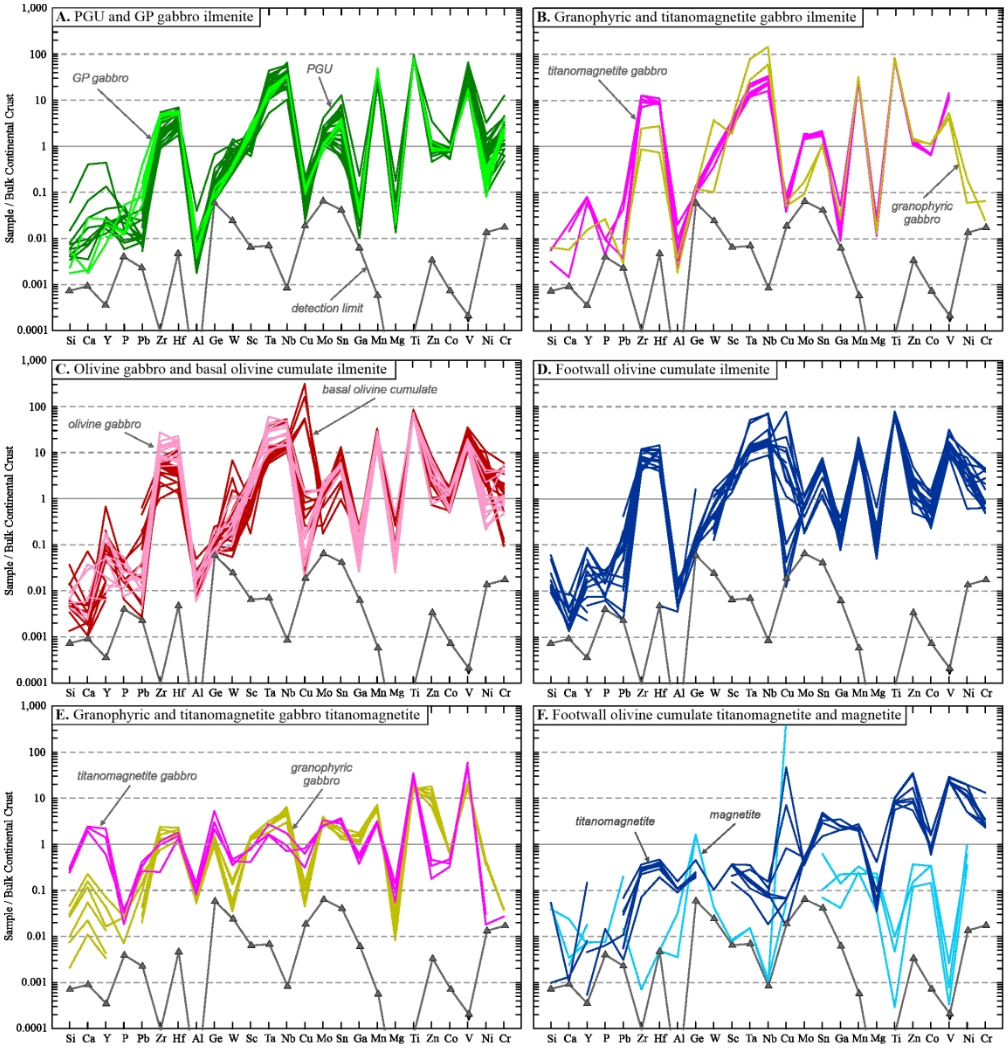

Figure 5. Multi-element diagrams of ilmenite (A-D) and titanomagnetite and magnetite (E-F). The elements are ordered by increasing compatibility into magnetite (see Dare et al. 2012) and normalised to the bulk continental crust (Rudnick & Gao 2003). The grey lines represent detection limits.

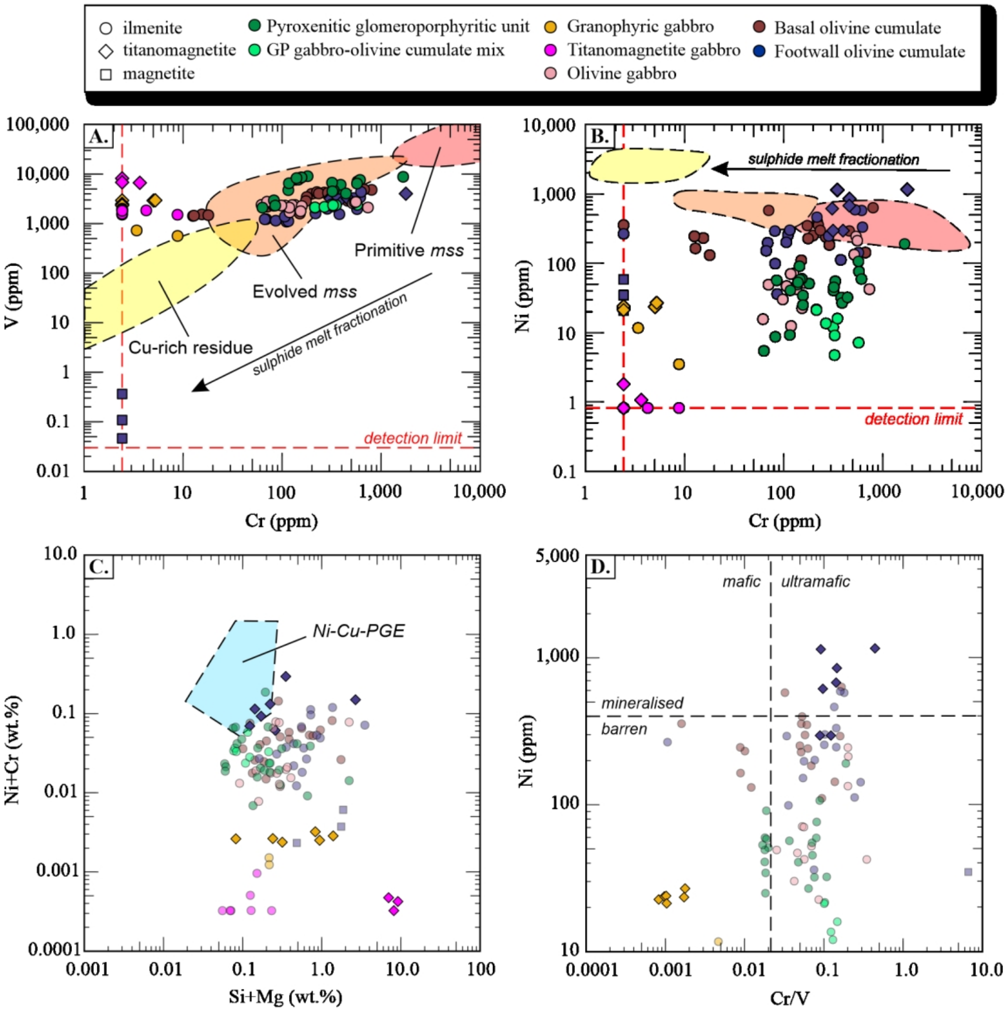

Figure 6. A-B. Cr versus V and Ni for Fe-Ti oxides. Stippled fields represent the compositional fields of Fe-Ti oxides exsolved from evolving sulphide melts (Dare et al. 2014). Red dashed lines correspond to detection limits. C. Si+Mg versus Ni+Cr deposit type discrimination diagram of Dupius & Beaudoin (2011). D. Cr/V versus Ni exploration discrimination diagram of Ward et al. (2018). Note how Fe-Ti oxides are most consistent with those derived from evolved mss and that titanomagnetite hosted in the ultramafic cumulates units are consistent with those derived from ultramafic-hosted Ni-Cu-(PGE) sulphide deposits.

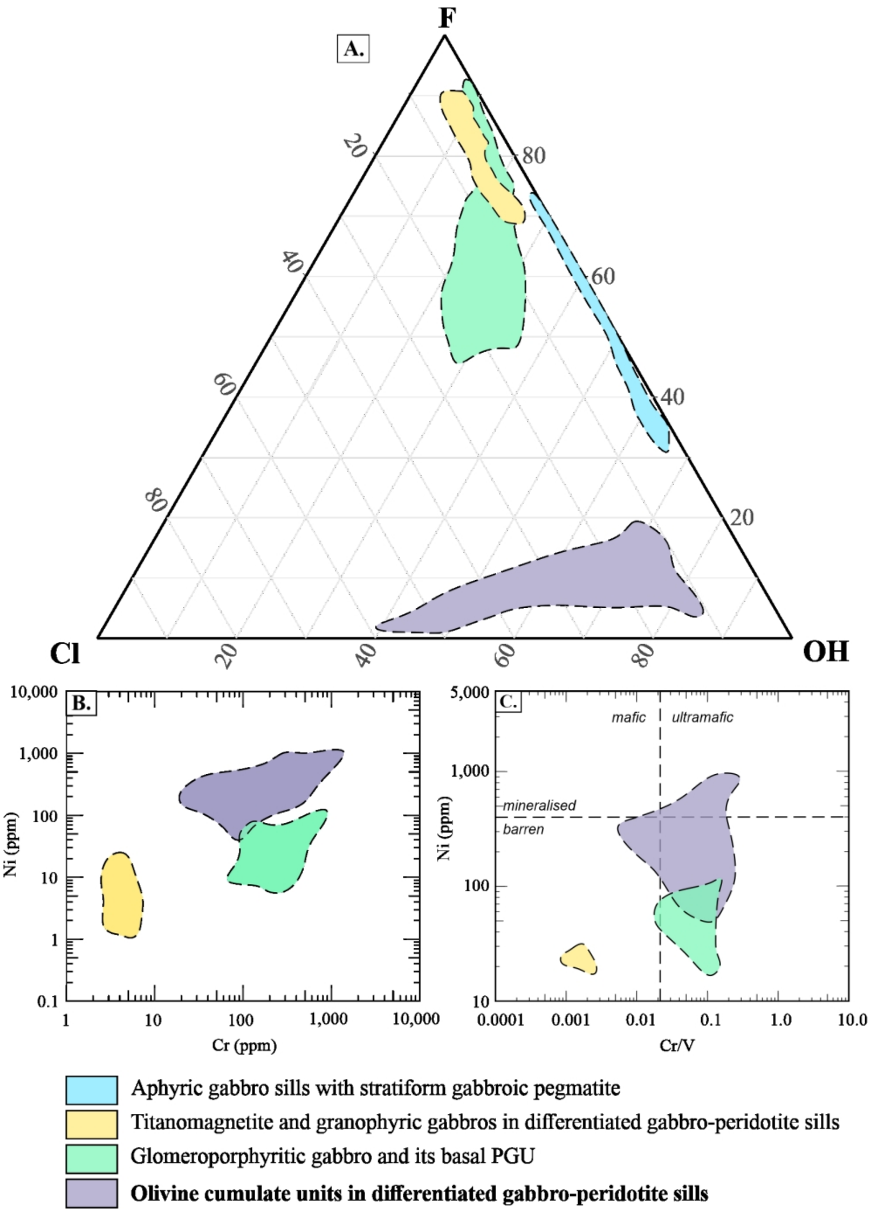

Figure 7. A. F-Cl-OH apatite ternary diagram with 95th percentile contours for apatite grains present in aphyric gabbro sills (light blue field), glomeroporphyritic gabbros (green field), titanomagnetite and granophyric gabbros (yellow field), and olivine cumulate units (dark blue field). Note that apatite grains indicating potential economic interest plot in the dark blue field. B. Cr versus Ni discrimination diagram for titanomagnetite and ilmenite in the Labrador Trough. C. Cr/V versus Ni discrimination diagram for titanomagnetite and ilmenite in the Labrador Trough (modified from Ward et al. 2018). Those that plot in the dark blue field are considered a good indication of proximal mineralised olivine cumulate units in the Labrador Trough

Table 1. Summary of EPMA apatite compositions

Location:	Idefix PGE-Cu prospect												Huckleberry Cu-Ni-(PGE) prospect			
Rock:	Aphyric gabbro (NS; *n* = 12)				Aphyric gabbro (DS; *n* = 14)				Aphyric gabbro (GS; *n* = 22)				PGU (GS; *n* = 37)			
Statistic:	*min*	*max*	*average*	*2SD*	*min*	*max*	*average*	*2SD*	*min*	*max*	*average*	*2SD*	*min*	*max*	*average*	*2SD*
Major elements wt.%																
CaO	53.7	55.7	54.8	1.24	54.8	56.2	55.4	0.79	53.4	55.6	54.5	1.39	53.0	56.0	55.1	1.21
P_2O_5	40.9	42.1	41.6	0.71	41.2	42.4	41.8	0.60	40.3	42.4	41.5	1.17	40.1	42.2	41.7	0.77
Na_2O	0.00	0.02	0.01	0.02	0.00	0.03	0.01	0.02	0.00	0.06	0.01	0.04	0.00	0.06	0.02	0.04
MgO	0.00	0.01	0.00	0.01	0.00	0.28	0.04	0.16	0.00	0.13	0.01	0.06	0.00	0.33	0.03	0.15
Al_2O_3	0.00	0.02	0.00	0.01	0.00	0.24	0.05	0.15	0.00	0.23	0.02	0.10	0.00	0.46	0.05	0.22
SiO_2	0.01	0.10	0.06	0.05	0.04	0.48	0.27	0.24	0.01	0.59	0.17	0.23	0.02	3.18	0.29	1.00
MnO	0.00	0.05	0.02	0.03	0.00	0.06	0.02	0.03	0.00	0.06	0.02	0.03	0.00	0.08	0.03	0.05
FeO	0.01	0.15	0.07	0.08	0.05	0.33	0.14	0.19	0.13	0.86	0.35	0.37	0.08	1.19	0.41	0.47
F	1.22	1.44	1.36	0.13	1.16	1.52	1.41	0.20	1.68	2.98	2.40	0.63	1.83	3.87	2.92	1.13
Cl	0.13	0.17	0.15	0.02	0.16	0.37	0.22	0.11	0.04	0.11	0.07	0.04	0.05	1.78	0.54	1.07
OH	1.09	1.22	1.14	0.08	1.07	1.23	1.12	0.10	0.43	1.01	0.70	0.30	0.05	0.62	0.38	0.28
Total	97.7	100.6	99.1	1.97	99.8	101.3	100.5	0.88	97.6	101.4	99.7	2.22	100.2	102.6	101.5	1.07
X_{Cl}	0.02	0.02	0.02	0.00	0.02	0.05	0.03	0.02	0.01	0.02	0.01	0.00	0.01	0.24	0.07	0.14
X_F	0.31	0.37	0.35	0.04	0.30	0.39	0.37	0.06	0.44	0.76	0.61	0.16	0.46	0.96	0.73	0.27
X_{OH}	0.60	0.66	0.63	0.04	0.58	0.67	0.61	0.06	0.23	0.55	0.38	0.16	0.03	0.33	0.20	0.15
O = F,Cl	0.55	0.64	0.60	0.05	0.54	0.68	0.64	0.09	0.72	1.27	1.03	0.27	1.12	1.66	1.35	0.28
Cl/F	0.09	0.13	0.11	0.02	0.10	0.27	0.15	0.09	0.02	0.04	0.03	0.02	0.01	0.97	0.23	0.53

Location:	Huckleberry Cu-Ni-(PGE) prospect															
Rock:	GP gabbro (DS; *n* = 11)				Hanging wall gabbro (NS; *n* = 11)				Basal ol cumulate (NTS; *n* = 20)				FW ol cumulate (NTS; *n* = 17)			
Sample:	*min*	*max*	*average*	*2SD*	*min*	*max*	*average*	*2SD*	*min*	*max*	*average*	*2SD*	*min*	*max*	*average*	*2SD*
Major elements wt.%																
CaO	54.0	55.8	54.7	1.57	54.0	55.0	54.4	0.64	47.0	56.4	54.1	5.60	47.5	56.2	54.6	3.04
P_2O_5	39.5	42.5	41.3	1.96	40.8	41.9	41.6	0.57	35.5	42.9	40.6	4.03	36.0	42.2	41.0	2.54
Na_2O	0.00	0.11	0.04	0.09	0.00	0.07	0.03	0.05	0.00	0.16	0.02	0.08	0.00	0.31	0.07	0.19
MgO	0.01	2.02	0.37	1.62	0.00	0.08	0.01	0.05	0.00	2.61	0.43	1.61	0.00	2.02	0.24	0.81
Al_2O_3	0.01	0.04	0.02	0.02	0.00	0.07	0.02	0.05	0.00	1.13	0.19	0.72	0.00	2.70	0.13	1.04
SiO_2	0.13	2.29	0.54	1.72	0.00	0.21	0.06	0.14	0.03	6.80	1.22	4.15	0.07	4.29	0.66	1.78
MnO	0.01	0.04	0.02	0.03	0.07	0.36	0.16	0.19	0.01	0.16	0.05	0.10	0.00	0.21	0.05	0.10
FeO	0.10	1.00	0.53	0.58	0.10	0.64	0.40	0.35	0.05	3.86	0.86	2.29	0.23	7.32	0.84	2.69

Table 1. Continued

F	0.24	2.28	1.40	1.62	3.20	3.66	3.43	0.31	0.07	0.83	0.39	0.49	0.01	3.18	1.11	2.37
Cl	1.00	3.13	1.69	1.57	0.05	0.54	0.24	0.34	0.76	4.61	1.99	2.40	0.26	3.90	1.91	2.37
OH	0.40	1.28	0.77	0.70	0.16	0.32	0.21	0.12	0.61	1.54	1.14	0.52	0.26	1.37	0.84	0.75
Total	100.3	104.1	101.4	2.80	99.4	101.1	100.5	0.99	98.7	102.6	101.0	2.20	99.8	104.1	101.5	1.50
X_{Cl}	0.14	0.43	0.23	0.21	0.01	0.07	0.03	0.04	0.11	0.65	0.28	0.33	0.03	0.54	0.26	0.33
X_F	0.06	0.57	0.35	0.40	0.80	0.91	0.86	0.07	0.02	0.21	0.10	0.13	0.00	0.80	0.28	0.59
X_{OH}	0.21	0.68	0.41	0.38	0.08	0.17	0.11	0.06	0.34	0.86	0.62	0.29	0.14	0.76	0.46	0.42
O = F,Cl	0.52	1.31	0.97	0.64	1.39	1.55	1.50	0.11	0.22	1.07	0.61	0.49	0.39	1.45	0.90	0.71
Cl/F	0.63	7.73	2.37	5.74	0.01	0.16	0.07	0.10	1.07	62.72	10.14	30.76	0.09	417.86	34.96	172.02

Location:	Huckleberry Cu-Ni-(PGE) prospect							
Rock:	Olivine gabbro (NS; *n* = 27)				Granophyric gabbro (NS; *n* = 16)			
Sample:	*min*	*max*	*average*	*2SD*	*min*	*max*	*average*	*2SD*
Major elements wt.%								
CaO	51.3	56.8	55.1	2.80	49.4	55.9	55.0	3.35
P_2O_5	39.1	42.6	41.4	1.87	38.4	42.5	41.7	2.03
Na_2O	0.00	0.09	0.02	0.04	0.02	0.11	0.07	0.05
MgO	0.00	2.89	0.28	1.16	0.01	0.07	0.03	0.03
Al_2O_3	0.00	0.32	0.05	0.14	0.00	0.19	0.04	0.11
SiO_2	0.10	3.39	0.50	1.29	0.11	0.31	0.18	0.10
MnO	0.00	0.05	0.02	0.03	0.06	0.14	0.11	0.05
FeO	0.08	1.35	0.51	0.60	0.29	0.86	0.63	0.38
F	0.22	2.25	1.20	1.51	2.75	3.39	3.03	0.45
Cl	0.25	4.06	1.05	1.77	0.33	0.60	0.48	0.16
OH	0.59	1.43	1.01	0.48	0.04	0.48	0.35	0.26
Total	97.3	103.5	101.2	3.38	92.6	103.3	101.6	5.50
X_{Cl}	0.03	0.57	0.15	0.25	0.04	0.08	0.06	0.02
X_F	0.06	0.56	0.30	0.37	0.68	0.91	0.75	0.13
X_{OH}	0.33	0.79	0.55	0.27	0.02	0.25	0.18	0.14
O = F,Cl	0.34	1.09	0.74	0.47	1.26	1.55	1.38	0.20
Cl/F	0.13	10.01	2.24	5.76	0.11	0.20	0.16	0.06

[1] DS = disseminated sulphides, GS = globular sulphides, NTS = net-textured sulphides, and NS = no sulphides.

Table 2. Summary of EPMA and LA-ICP-MS Fe-Ti oxide compositions from Huckleberry. DL = detection limits in ppm.

	Rock type:	**PGU**				**GP gabbro-olivine cumulate**				**Granophyric gabbro**							
	Mineral:	Ilmenite (*n* = 23)				Ilmenite (*n* = 8)				Ilmenite (*n* = 2)				Titanomagnetite (*n* = 6)			
	Mineralisation:	Gb sulphides				NT sulphides				Non-mineralised							
DL	Element	Av.	2σ	Min	Max	Av.	2σ	Min	Max	Av.	2σ	Min	Max	Av.	2σ	Min	Max
EPMA analyses (wt.%)																	
	Fe_2O_3	2.1	1.9	0.3	3.7	3.2	1.5	0.3	5.1	4.7	2.8	3.2	6.9	40.8	4.4	38.1	45.2
	FeO	42.2	3.2	39.8	44.5	40.4	0.6	39.5	41.2	41.8	2.4	40.3	43.0	42.7	1.7	41.4	43.7
LA-ICP-MS analyses (ppm)																	
0.113	^{24}Mg	829	1879	378	4927	594	47	560	630	400	152	346	454	535	563	232	982
0.510	^{27}Al	486	1308	148	3335	510	431	313	992	237	231	155	319	4949	734	4446	5366
212.8	^{29}Si	2280	7295	213	17288	687	1148	213	1641	1765	168	1706	1824	5807	9520	589	12965
2.340	^{31}P	8.4	15.6	2.3	28.2	10.3	21.0	2.3	30.1	8.7	18.1	2.3	15.1	6.9	12.8	2.3	15.5
43.4	^{44}Ca	1810	8174	43	18571	358	882	43	1274	575	885	262	888	4498	7730	507	10389
0.146	^{45}Sc	29.5	26.1	10.1	61.3	49.2	24.0	34.5	67.6	61.9	58.6	41.2	82.6	29.2	3.7	27.4	32.2
0.400	^{49}Ti	364878	41082	335340	412300	343395	21134	325784	362454	351127	28342	341106	361147	72209	12150	63518	81391
0.030	^{51}V	6338	4287	2100	9050	2272	267	2092	2440	646	231	564	728	2668	602	2331	2953
2.421	^{52}Cr	318	681	63	1671	324	226	215	573	6	8	3	9	3	3	2	5
0.462	^{55}Mn	26842	13408	17264	35067	36887	1440	35782	37982	24888	289	24785	24990	5085	1120	4209	5583
0.020	^{59}Co	21.9	8.5	13.8	30.8	21.9	1.0	21.1	22.7	29.9	1.7	29.3	30.5	17.6	1.1	17.1	18.4
0.821	^{60}Ni	52.6	77.8	5.5	191.0	13.2	12.4	4.7	21.7	7.6	11.6	3.5	11.7	23.7	3.7	21.3	26.9
0.522	^{63}Cu	2.3	3.1	0.7	6.0	3.1	1.2	2.5	4.2	1.5	0.4	1.4	1.7	2.1	2.0	1.2	3.8
0.250	^{66}Zn	81.6	80.5	33.1	251.7	66.4	22.6	55.6	90.3	100.8	16.8	94.9	106.7	863.0	598.1	478.5	1304.7
0.102	^{71}Ga	0.72	1.39	0.10	3.60	0.67	0.23	0.46	0.83	0.44	0.06	0.41	0.46	22.13	9.93	15.66	28.26
0.079	^{74}Ge	0.20	0.34	0.08	0.87	0.13	0.07	0.08	0.17	0.16	0.00	0.16	0.16	1.57	0.59	1.18	1.95
0.104	^{75}As	0.19	0.81	0.10	2.04	0.10	0.00	0.10	0.10	0.10	0.00	0.10	0.10	0.10	0.00	0.10	0.10
0.007	^{89}Y	0.96	3.42	0.19	8.38	0.31	0.27	0.15	0.49	0.24	0.15	0.18	0.29	0.48	1.02	0.06	1.36
0.013	^{90}Zr	315	519	120	1273	598	138	475	676	217	293	114	321	206	160	99	315
0.007	^{93}Nb	274	228	83	523	275	23	251	285	812	954	474	1149	39	18	24	51
0.053	^{95}Mo	1.55	1.01	0.84	3.30	0.79	0.24	0.58	0.95	0.10	0.09	0.07	0.13	2.65	0.68	2.29	3.19
0.072	^{118}Sn	6.06	10.66	0.83	21.70	5.59	1.96	4.32	6.83	1.84	0.24	1.76	1.93	2.79	1.18	2.22	3.78
0.047	^{121}Sb	0.06	0.05	0.05	0.13	0.05	0.02	0.05	0.07	0.05	0.00	0.05	0.05	0.07	0.05	0.05	0.12
0.007	^{139}La	0.11	0.27	0.01	0.63	0.02	0.01	0.01	0.03	0.04	0.06	0.02	0.06	0.14	0.16	0.03	0.22
0.024	^{172}Yb	0.63	0.74	0.07	1.38	0.51	0.40	0.34	0.80	0.63	1.00	0.28	0.99	0.07	0.09	0.03	0.13
0.018	^{178}Hf	15.5	15.8	6.5	42.1	20.0	2.3	18.2	21.6	6.4	10.5	2.7	10.1	6.4	2.9	4.5	8.4
0.005	^{181}Ta	14.6	12.1	3.7	30.7	10.3	3.8	7.5	13.0	36.9	50.1	19.1	54.6	1.7	0.6	1.3	2.2
0.025	^{182}W	0.67	0.59	0.26	1.43	0.35	0.11	0.24	0.44	1.89	5.06	0.10	3.68	0.08	0.11	0.03	0.16
0.026	^{208}Pb	0.16	0.24	0.03	0.47	1.61	2.37	0.58	4.28	0.05	0.04	0.03	0.06	1.01	1.76	0.22	2.49
n/a	Ni/Cr	0.23	0.35	0.07	0.67	0.05	0.07	0.01	0.10	1.92	4.31	0.40	3.45	7.95	4.79	4.67	9.90

Table 2. Continued

Rock type:	**Titanomagnetite gabbro**								**Olivine gabbro**				**Basal olivine cumulate**			
Phase:	Ilmenite (*n* = 7)				Titanomagnetite (*n* = 3)				Ilmenite (*n* = 13)				Ilmenite (*n* = 18)			
Mineralised:	Non-mineralised								Ds sulphides				NT sulphides			
Element	Av.	2σ	Min	Max	Av.	2σ	Min	Max	Av.	2σ	Min	Max	Av.	2σ	Min	Max
Fe_2O_3	7.6	3.6	5.0	11.3	49.8	2.0	48.5	50.9	11.7	4.7	6.8	16.3	9.4	4.2	0.0	15.5
FeO	41.1	2.0	39.1	42.5	37.6	0.6	37.2	37.8	38.1	2.3	35.0	40.6	40.0	1.9	36.6	44.6
^{24}Mg	454	278	322	731	2674	2416	1546	3948	2186	5646	693	11760	2900	5655	774	9395
^{27}Al	607	1032	181	1693	9100	5265	6720	11928	1191	837	499	1869	1298	1662	638	4127
^{29}Si	738	1098	213	1596	78400	19344	68460	87780	1838	5198	213	10458	1935	5349	213	10360
^{31}P	6.3	15.8	2.3	23.9	16.9	11.6	10.5	21.8	10.1	16.7	2.3	30.3	6.9	15.3	2.3	25.9
^{44}Ca	300	720	43	953	101920	23495	88620	110880	301	1058	43	1726	278	1499	43	3271
^{45}Sc	69.1	17.0	55.4	76.9	14.6	9.8	9.0	18.2	50.5	29.2	22.1	77.4	30.8	47.6	3.8	72.0
^{49}Ti	339540	10546	330540	344820	135520	29030	120540	149520	298106	23962	278702	322065	318459	46739	282277	368874
^{51}V	1788	353	1512	2003	7225	1677	6670	8190	2321	645	1697	2770	3056	2624	1428	4891
^{52}Cr	4	5	2	9	3	1	2	4	250	457	62	736	223	449	2	802
^{55}Mn	21726	664	21168	22176	2290	289	2176	2453	16228	8233	9691	22386	17397	8166	10185	25544
^{59}Co	17.8	1.0	17.2	18.5	10.4	3.9	8.6	12.5	30.3	20.1	13.4	42.5	23.1	21.8	13.3	48.6
^{60}Ni	0.8	0.0	0.8	0.8	1.2	1.0	0.8	1.8	74.9	144.4	12.5	245.3	288.9	284.9	110.6	633.6
^{63}Cu	1.6	0.9	1.0	2.2	15.7	13.6	8.4	21.8	9.5	29.3	0.5	39.9	951.7	4300.6	0.6	8341.0
^{66}Zn	94.6	20.2	78.5	106.3	23.5	20.4	12.9	33.2	273.1	302.3	54.0	549.8	251.7	309.5	52.7	621.0
^{71}Ga	0.34	0.45	0.14	0.83	7.88	3.46	6.08	9.53	1.46	1.77	0.42	3.45	2.74	1.33	0.98	3.98
^{74}Ge	0.15	0.05	0.12	0.18	4.54	4.24	2.77	6.89	0.12	0.12	0.08	0.27	0.12	0.12	0.08	0.32
^{75}As	0.10	0.00	0.10	0.10	0.10	0.00	0.10	0.10	0.10	0.00	0.10	0.11	0.12	0.09	0.10	0.29
^{89}Y	1.35	0.44	1.06	1.57	26.56	30.03	11.51	41.54	1.19	2.56	0.07	3.45	1.85	5.85	0.12	12.73
^{90}Zr	1373	525	941	1693	105	126	33	152	1506	1557	664	3621	636	492	132	1039
^{93}Nb	206	96	129	268	9	9	6	14	239	221	114	397	194	256	81	423
^{95}Mo	1.32	0.25	1.16	1.53	2.24	0.78	1.97	2.69	1.34	0.49	0.76	1.84	0.81	0.66	0.14	1.30
^{118}Sn	3.30	0.76	2.86	3.70	5.55	1.52	4.75	6.26	9.34	2.26	6.57	10.44	13.01	14.18	1.62	22.35
^{121}Sb	0.08	0.10	0.05	0.18	0.08	0.06	0.06	0.11	0.28	0.57	0.05	1.01	0.06	0.09	0.05	0.23
^{139}La	0.03	0.04	0.01	0.07	0.66	0.46	0.50	0.93	0.10	0.36	0.01	0.70	0.28	0.83	0.01	1.36
^{172}Yb	2.09	0.47	1.78	2.52	4.16	3.76	2.13	5.84	0.97	1.89	0.13	2.80	1.06	2.88	0.03	4.53
^{178}Hf	34.0	7.1	30.4	41.0	5.7	1.8	4.9	6.7	46.4	43.1	19.5	84.6	19.4	26.6	4.9	43.5
^{181}Ta	11.7	6.7	8.3	16.0	1.4	0.9	1.1	1.9	17.5	21.0	6.7	41.8	11.4	17.6	4.1	29.9
^{182}W	0.62	0.25	0.36	0.74	0.42	0.12	0.35	0.47	0.31	0.53	0.10	1.14	0.79	3.28	0.05	6.77
^{208}Pb	0.21	0.57	0.03	0.75	3.69	1.69	2.89	4.58	0.12	0.24	0.03	0.46	1.13	3.84	0.03	7.02
Ni/Cr	0.28	0.20	0.09	0.34	0.46	0.50	0.29	0.75	0.35	0.37	0.06	0.70	12.40	68.27	0.21	147.21

Table 2. Continued

Rock type:	**Footwall olivine cumulates**											
Phase:	Ilmenite (*n* = 16)				Titanomagnetite (*n* = 7)				Magnetite (*n* = 3)			
Mineralised:	NT sulphides											
Element	Av.	2σ	Min	Max	Av.	2σ	Min	Max	Av.	2σ	Min	Max
Fe_2O_3	10.7	7.0	3.0	18.6	47.0	9.7	41.1	56.8	69.6	0.9	69.0	70.4
FeO	40.1	3.7	35.9	42.7	38.7	4.2	34.0	41.0	31.4	0.4	31.1	31.8
^{24}Mg	4835	7841	1406	18186	2934	7687	953	11552	4208	5752	1001	6560
^{27}Al	835	551	359	1459	9437	3453	7578	13140	1126	2731	299	2702
^{29}Si	3073	8302	213	16887	2697	11013	238	15162	9501	10145	3835	13618
^{31}P	6.9	10.1	2.3	16.0	3.4	4.4	2.3	8.2	3.0	2.2	2.3	4.3
^{44}Ca	122	240	43	429	46	13	43	61	475	1067	157	1091
^{45}Sc	64.8	34.1	30.2	87.7	6.8	3.9	3.3	8.0	0.2	0.0	0.1	0.2
^{49}Ti	294205	51413	259800	342936	35873	13504	24075	44511	21	41	1	43
^{51}V	2021	1917	1094	4372	3460	684	3177	4023	0	0	0	0
^{52}Cr	247	445	2	627	583	1063	310	1780	2	0	2	2
^{55}Mn	11746	5703	7177	16671	1698	430	1510	2119	209	86	178	257
^{59}Co	16.7	19.8	6.1	39.7	27.1	22.6	15.9	44.4	7.3	6.0	3.9	9.2
^{60}Ni	267.0	323.0	36.1	591.8	720.5	713.5	296.0	1160.4	38.0	38.1	20.8	58.5
^{63}Cu	378.8	1396.9	0.3	2121.7	211.9	937.9	0.5	1263.5	6307	13902	1.4	13761
^{66}Zn	154.2	170.2	35.8	368.1	1205.2	1791.2	391.3	2541.4	15.3	19.4	8.5	26.4
^{71}Ga	2.54	2.80	1.23	6.26	39.86	15.28	32.49	55.42	2.18	2.93	0.67	3.59
^{74}Ge	0.12	0.09	0.08	0.20	0.32	0.24	0.25	0.59	1.44	2.35	0.08	2.12
^{75}As	0.10	0.00	0.10	0.11	0.11	0.01	0.10	0.11	0.10	0.00	0.10	0.10
^{89}Y	0.56	0.98	0.07	1.67	0.46	2.07	0.01	2.81	0.10	0.11	0.04	0.14
^{90}Zr	1054	693	526	1591	34	24	9	48	0	0	0	0
^{93}Nb	216	346	71	578	1	1	0	1	0	0	0	0
^{95}Mo	0.51	0.52	0.05	0.95	0.34	0.11	0.28	0.41	0.05	0.00	0.05	0.05
^{118}Sn	8.73	7.57	1.68	13.18	6.31	4.11	2.54	8.27	0.45	1.05	0.12	1.06
^{121}Sb	0.16	0.61	0.05	1.28	0.05	0.00	0.05	0.05	0.05	0.02	0.05	0.06
^{139}La	0.37	0.82	0.01	1.44	0.11	0.48	0.01	0.66	0.02	0.02	0.01	0.03
^{172}Yb	0.42	0.81	0.02	1.46	0.08	0.29	0.02	0.41	0.02	0.00	0.02	0.02
^{178}Hf	30.4	23.2	14.9	53.9	1.3	0.7	0.7	1.7	0.0	0.0	0.0	0.0
^{181}Ta	13.7	20.8	4.6	36.4	0.1	0.1	0.1	0.2	0.0	0.0	0.0	0.0
^{182}W	0.63	0.97	0.13	1.60	0.04	0.06	0.03	0.10	0.03	0.02	0.03	0.04
^{208}Pb	0.84	2.34	0.03	4.68	0.25	0.52	0.03	0.75	0.99	2.15	0.16	2.21
Ni/Cr	8.35	54.39	0.25	110.25	1.56	1.84	0.65	3.27	15.71	15.72	8.59	24.14